



CM-P00063983

ORGANIZATION FOR NUCLEAR RESEARCH

INCLUSIVE INTERACTIONS OF HIGH-ENERGY NEUTRINOS
AND ANTINEUTRINOS IN IRON

J.G.H. de Groot, T. Hansl, M. Holder, J. Knobloch, J. May, H.P. Paar,
P. Palazzi, A. Para, F. Ranjard, D. Schlatter, J. Steinberger,
H. Suter, W. von Rüden, H. Wahl, S. Whitaker and E.G.H. Williams
CERN, Geneva, Switzerland

F. Eisele, K. Kleinknecht, H. Lierl, C. Spahn
and H.J. Willutzki

Institut für Physik^{*)} der Universität, Dortmund, Germany

W. Dorth, F. Dydak, C. Geweniger, V. Hepp, K. Tittel and J. Wotschack,
Institut für Hochenergiephysik^{*)} der Universität, Heidelberg, Germany

P. Bloch, B. Devaux, S. Loucatos, J. Maillard,
B. Peyaud, J. Rander, A. Savoy-Navarro and R. Turley
D.Ph.P.E., CEN-Saclay, France

F.L. Navarria
Istituto di Fisica dell'Università, Bologna, Italy

ABSTRACT

We present results on charged current inclusive neutrino and antineutrino scattering in the neutrino energy range 30-200 GeV. The results include

- a) total cross-sections;
- b) y distributions;
- c) structure functions; and
- d) scaling violations observed in the structure functions.

The results, as well as their comparison with the results of electron and muon inclusive scattering, are in agreement with the expectations of the quark parton model and QCD.

Geneva - 24 November 1978

(Submitted to Zeitschrift für Physik)

^{*)} Supported by the Bundesministerium für Forschung und Technologie.

1. INTRODUCTION

1.1 Deep inelastic lepton scattering

The study of inclusive neutrino-nucleon scattering is of interest chiefly in connection with the problem of the structure of the nucleon and the weak interactions of its constituents. Neutrinos and antineutrinos are excellent projectiles for exploring the interior of the nucleon, on the one hand because of their ease of penetration, undamped by propagators at presently available momentum transfers, and on the other hand because the chiral nature of the weak interaction makes it possible to separate the effects of "particles" and "antiparticles" among the nucleon constituents.

The basis of all phenomenological analysis is the diagram of Fig. 1, which illustrates the assumption that the interaction is of the current-current form; the neutrino changes to a muon at one vertex, momentum is transferred, perhaps through the mediation of a heavy vector boson, to the second vertex, where the nucleon is transformed to the final hadronic system. The kinematics of the inclusive process can be described by the three variables E_ν , $Q^2 = -(k - k')^2$, and $\nu = p \cdot (k - k') \approx ME_h$, or alternatively, E_ν , x , and y , where $x = Q^2/2\nu$ and $y = \nu/p \cdot k$. Here E_ν is the energy of the incident neutrino, E_h is the energy of the outgoing hadron state, M is the nucleon mass, and the other variables are defined in Fig. 1. y is the fractional neutrino energy transferred to the hadrons, the so-called "inelasticity", and x is the fraction of the maximum momentum transfer possible for the particular y . Both x and y range from zero to one. If the usual V-A current is assumed at the lepton vertex, and if initial and final hadron polarizations are summed, the inclusive cross-section corresponding to the diagram of Fig. 1 can be written in terms of three structure functions:

$$\frac{d^2\sigma}{dx dy} = \frac{G^2 ME_\nu}{\pi} \left[(1 - y)F_2(Q^2, \nu) + xy^2F_1(Q^2, \nu) \pm \left(y - \frac{y^2}{2}\right)xF_3(Q^2, \nu) \right]. \quad (1)$$

The upper sign refers to neutrinos, the lower to antineutrinos. In general, the form factors are not the same for neutrinos and antineutrinos. However, for charge symmetric nuclei (Fe is nearly charge symmetric), and with the assumption

of charge symmetry in the neutrino nucleon interaction, that is $F_1^{\nu p}(x) = F_1^{\bar{\nu} n}(x)$, and $F_1^{\bar{\nu} p}(x) = F_1^{\nu n}(x)$, the neutrino and antineutrino structure functions are equal, and the total number of structure functions reduce to three.

1.2 Scaling

In earlier electron [1] and neutrino [2] inelastic scattering experiments it has been observed that, at least within certain experimental uncertainties, the cross-sections are consistent with Bjorken scaling [3]; that is, that the structure functions depend only on the dimensionless variable $x = Q^2/2\nu$ instead of varying with both Q^2 and ν : $F_1(Q^2, \nu) \rightarrow F_1(x)$. To the extent that scaling is valid, and propagator effects are negligible, the neutrino cross-sections are therefore expected to be proportional to neutrino energy, and the x and y distributions are expected to be independent of neutrino energy. One of the aims of the present experiment is to test this hypothesis at higher energies and with good precision.

1.3 Quark parton model

A dynamical model of the nucleon which gives rise to scaling is the so-called naive quark parton model [4]. It is assumed that the nucleon constituents responsible for weak and electromagnetic interactions are the quarks of spin one half and third integral electric charge. It is further assumed that these quarks are effectively free and that their weak interactions are identical to the lepton weak interactions, except for the Cabibbo rotation.

The quark constituency of the nucleon, in this model, is thought to be composed of three valence quarks: two up and one down quark for the proton, two down and one up quark for the neutron, plus a "sea" of quark-antiquark pairs. This sea contains $\bar{u}u$, $\bar{d}d$, $\bar{s}s$, and $\bar{c}c$ pairs, where U, D, S, and C stand for up, down, strange, and charmed quarks. Let $u(x)$, $d(x)$, $s(x)$, and $c(x)$ ($\bar{u}(x)$, $\bar{d}(x)$, $\bar{s}(x) = s(x)$, and $\bar{c}(x) = c(x)$) be the distributions in the fractional nucleon momentum carried by the respective quarks (and antiquarks) in the proton. In terms of these distributions, and the distributions

$$q(x) = u(x) + d(x) + s(x) + c(x)$$

and

$$\bar{q}(x) = \bar{u}(x) + \bar{d}(x) + \bar{s}(x) + \bar{c}(x) ,$$

and for charge symmetric nuclei,

$$2xF_1(x) = F_2^V(x) = F_2^{\bar{V}}(x) = q(x) + \bar{q}(x)$$

$$xF_3^V(x) = q(x) - \bar{q}(x) + 2\bar{s}(x) - 2\bar{c}(x)$$

$$xF_3^{\bar{V}}(x) = q(x) - \bar{q}(x) - 2\bar{s}(x) + 2\bar{c}(x) .$$

The relation $2xF_1 = F_2$ is a consequence of the spin $\frac{1}{2}$ nature of the quark constituents [5]. The valence quark distribution $q(x) - \bar{q}(x)$ is the average of the neutrino and antineutrino structure functions xF_3^V and $xF_3^{\bar{V}}$. In this model the inclusive cross-sections [1] are:

$$\frac{d^2\sigma^V}{dx dy} = \frac{G^2 ME_V}{\pi} \left\{ [q(x) + s(x)] + (1-y)^2 [\bar{q}(x) - \bar{s}(x)] \right\} \quad (2)$$

$$\frac{d^2\sigma^{\bar{V}}}{dx dy} = \frac{G^2 ME_V}{\pi} \left\{ (1-y)^2 [q(x) - s(x)] + [\bar{q}(x) + \bar{s}(x)] \right\} . \quad (2')$$

Here, and in the following, we ignore the contributions of $c(x)$ and $\bar{c}(x)$ which are expected to be small, owing to the larger mass of the charmed quark. It can be seen from (2) and (2'), that:

- a) At small y , and at all y to the extent that the strange sea can be neglected, the sum of neutrino and antineutrino scattering measures directly the total quark distribution, $q + \bar{q} = F_2$:

$$\frac{d^2\sigma^V}{dx dy} + \frac{d^2\sigma^{\bar{V}}}{dx dy} = \frac{G^2 ME_V}{\pi} [1 + (1-y)^2] [q(x) + \bar{q}(x)] \quad (3)$$

- b) The difference of neutrino and antineutrino cross-sections measures directly the valence quark distribution, $q - \bar{q} = xF_3$:

$$\frac{d^2\sigma^V}{dx dy} - \frac{d^2\sigma^{\bar{V}}}{dx dy} = \frac{G^2 ME_V}{\pi} [1 - (1-y)^2] [q(x) - \bar{q}(x)] . \quad (4)$$

- c) At large y the neutrino cross-section measures the quark distribution:

$$\left. \frac{d^2\sigma^V}{dx dy} \right|_{y \rightarrow 1} = \frac{G^2 ME_V}{\pi} [q(x) + s(x)] , \quad (5)$$

- d) At large y the antineutrino cross-section measures directly the $\bar{q}(x) + \bar{s}(x)$ antiquark sea:

$$\left. \frac{d^2\sigma}{dx dy} \right|_{y \rightarrow 1} = \frac{G^2 M E_\nu}{\pi} [\bar{q}(x) + \bar{s}(x)] . \quad (6)$$

The total fractional nucleon momentum carried by the sum of quarks and antiquarks is given by

$$Q + \bar{Q} = \int_0^1 F_2 dx = \int_0^1 [q(x) + \bar{q}(x)] dx . \quad (7)$$

It need not be one, since part of the nucleon momentum may be carried by the gluons which are supposed to bind the quarks, and which are supposed not to have weak and electromagnetic interactions.

Among the consequences of this naive quark parton model are the following:

- a) The cross-sections rise linearly with neutrino energy.
b) The number of independent form factors reduce to two, in virtue of the Callan-Gross relation [5]:

$$2xF_1 = F_2 . \quad (8)$$

- c) The Gross-Llewellyn Smith sum rule [6]:

$$\int F_3 dx = 3 . \quad (9)$$

This sum rule expresses the fact that the number of valence quarks per nucleon is three.

- d) The F_2 form factors measured in electron, muon, and neutrino inclusive scattering should be the same, except for those differences due to the inequality of the electromagnetic and weak charges:

$$F_2^{e,d}(x) = F_2^{\mu,d}(x) = \frac{5}{18} \left\{ 1 - \frac{3}{5} \frac{(s + \bar{s})}{(q + \bar{q})} \right\} F_2^{\nu,d}(x) . \quad (10)$$

The second term is a correction of the order of 5% on the average, and up to 20% at small x for an SU(3) symmetric sea.

In summary, neutrino inclusive scattering experiments offer several possibilities for critical experimental checks of the quark parton model, and also the

possibility to measure the quark and antiquark structure functions *independently*. At present, the existence of quarks has not been demonstrated. It will be seen in the following, however, that the quark parton model gives a good representation of our results and we have adopted the language of this model throughout.

1.4 Scale breaking and QCD

Deviations from scaling have been observed in inclusive electron, muon and neutrino scattering [7]. These are of course in disagreement with the naive quark parton model, but some scaling violations must be expected from such threshold effects as the onset of charm production.

Scaling violations are also predicted in the "quantum chromodynamic" (QCD) field theory of the strong interactions of the quarks. In QCD the deviations from scaling at high momentum transfer can be calculated, because in this theory the interaction strength becomes weak with increasing Q^2 , so that for $Q^2 \gtrsim 1 \text{ GeV}^2$ perturbative calculations are thought to be justifiable. If the three structure functions for valence quarks, sea quarks, and gluons are known for some Q^2 , then QCD predicts how these distributions evolve with Q^2 . Qualitatively, as Q^2 increases, the relative contribution of the sea quarks is expected to increase and all structure functions are expected to concentrate towards smaller x . Unfortunately for the quantitative predictions, the gluon distribution is experimentally unknown at any Q^2 and cannot be measured in lepton scattering directly. It affects the predictions for the Q^2 evolution of $F_2(x)$ seriously, so that theoretical assumptions about this distribution must be made. However, the QCD predictions for the valence quark distribution $x F_3(x, Q^2)$ are independent of the gluon distribution, and are therefore more reliable.

Inclusive lepton scattering experiments at high momentum transfer can provide the possibility of experimental confrontation of these theoretical predictions. Neutrino experiments have here two important advantages over charged lepton experiments:

- i) The valence and sea structure functions can be measured independently, whereas only their sum $F_2(x, Q^2)$ can be measured in the case of charged leptons.

- ii) The cross-sections at large Q^2 can be measured more readily because the propagator effect is negligible (high mass of the intermediate boson).
- iii) The flavour content of the sea can be measured because there are flavour changing currents.

1.5 Content of this paper

The experimental results reported here are based on data obtained early in 1977 in 200 GeV narrow-band ν and $\bar{\nu}$ beams at the CERN SPS. In Sections 2 and 3 the experimental conditions are described. In Sections 4, 5, and 6 total cross-sections, y-distributions and x-distributions (structure functions) are presented, respectively, and compared with the predictions of the quark parton model. In Section 7 the experimental results relevant to scaling violations are presented and compared with calculations based on QCD.

2. THE NEUTRINO BEAM

The results described in the following were obtained in the CERN SPS narrow-band neutrino beam. Secondaries produced in the interaction of 400 GeV protons in beryllium, in a 10^{-5} steradian cone about the forward direction, are sign and momentum selected to 200 ± 10 GeV/c. They are then focused to a pencil beam with ± 0.2 mrad divergence, and enter an evacuated decay pipe 1.2 m in diameter and 300 m long. A steel shield 2.5 m in diameter and 172 m long follows the decay pipe, with provision for sampling the muon flux in eight different positions. These muon measurements provide an absolute monitor of the neutrino flux [8].

Additional monitoring devices are:

- a) Segmented ionization chambers before and after the decay tunnel, as well as after the first 10 m of iron shield.
- b) A beam current transformer (BCT) which measures the absolute hadron flux immediately before the decay tunnel, with an accuracy of a few per cent.
- c) A Čerenkov counter of novel design to measure the hadron beam composition, in front of the decay tunnel.
- d) A thermal calorimeter between the decay tunnel and the shield. This is an insulated iron block, ~ 50 cm in diameter and 2 m long, in which the hadron

beam is absorbed. The temperature of the block and the surrounding shield are periodically recorded and permit an absolute determination of the hadron energy flux with an accuracy of $\sim 5\%$.

Ninety-eight per cent of the neutrino flux is due to the two-body decays $\pi \rightarrow \mu + \nu$ and $K \rightarrow \mu + \nu$. For these neutrinos, the energy can be inferred from the hadron decay angle, as determined from the beam geometry and the radial displacement of the event from the beam axis. This energy is of course subject to the two-fold ambiguity of the neutrino parent. The neutrino energy uncertainty is in general rather large, larger in fact than the uncertainty in the measured muon and hadron energies of the observed events. Consequently, the latter are used in the data reduction. The *a priori* knowledge of the neutrino energy is however very valuable in that it permits checks on the absolute calibration of the measurements and the resolutions. In Fig. 2 a scatter plot of measured event energy versus detection radius is shown for a sample of neutrino events, to illustrate this kinematic property of the beam. Figure 3 shows the calculated neutrino and antineutrino energy spectra. The spectrum from very low energies to the maximum of ~ 200 GeV is covered in the experiment, and the shape is determined by simple geometric considerations, except for a single number which must be measured for each beam condition: the ratio of kaons to pions.

3. DETECTOR

The detector (see Fig. 4) consists of circular, toroidally magnetized iron plates, 3.75 m outer diameter, 30 cm inner diameter, grouped into 19 modules, each containing plates with a total thickness of 75 cm, and weighing ~ 65 tons. Between the modules are triple-plane drift chambers [9], with wires in the horizontal direction and at $\pm 60^\circ$ to the horizontal. Between each pair of iron plates, a plane of eight horizontal scintillators is placed, in order to measure the ionization generated by the hadron shower, as well as for triggering purposes. The first seven modules consist of 5 cm thick iron plates, the remainder of 15 cm thick plates. Details of the detector [10] and the hadron energy resolution and calibration [11] are published. The apparatus is triggered whenever either

more than 3 GeV are deposited in adjacent modules in the calorimeters, or three or more calorimeter modules have a signal of minimum ionization or more. It takes about 3 μ sec to store an event in a buffer of 40-event capacity. The beam was run in a fast-ejection mode, in which the spill time corresponds to one SPS revolution of 23 μ sec. The dead-time is monitored. The hadron shower is calculated from the observed pulse heights in a depth of 1.5 m of iron following the event vertex, after correction for the pulse height contributed by the muon. The resolution of the calorimeter is $\sim \sqrt{1 \text{ GeV}/E_h}$ for 5 cm sampling, and $\sim \sqrt{3}$ times larger for 15 cm sampling. The muon momentum is calculated from the observed magnetic deflection, and is corrected for the observed radiation after the first 1.5 m of iron. The momentum resolution $\Delta p/p$ is limited by multiple scattering and is independent of momentum; for average length tracks it is $\pm 9\%$.

The pulse-height circuits are calibrated every few hours with test signals, and the phototube gains are monitored and updated continuously on the basis of cosmic ray muon data. Of the order of ten such muon events are recorded between machine bursts.

The data are selected and reconstructed by computer without manual intervention. In the off-line analysis, events are accepted if the following requirements are satisfied:

- 1) Hits are registered in at least two of the three planes in at least five consecutive chambers.
- 2) The reconstructed muon momentum is at least 7 GeV/c.
- 3) The origin of the event is between the 3rd plate of the first and the end of the eleventh module, so that a minimum of seven modules and an average of thirteen modules is available for muon momentum measurement.
- 4) The origin of the event is within a cylinder of 1.6 m radius centred on the detector axis, so that there are always at least 160 g/cm² of material for the lateral development of the shower and the correct measurement of the hadron energy.

- 5) The event origin is outside a geometrical area shown in Fig. 5 centred on the detector axis. This excluded region is somewhat different for the 5 cm and 15 cm modules. This region is excluded because muons of central origin and very small production angle propagate in a field-free region where their momentum can therefore not be measured, and because the measurement of the energy of hadron showers developing in this region suffers from cuts in the central scintillators, cuts necessitated by the presence of the magnetizing coils, and, in the case of the 5 cm modules, by spacers which maintain the gap between the plates.

It is noted that event selection is based on the muon only, so that the acceptance is independent of the existence or energy of a hadron shower.

On the basis of a hand-scanned and reconstructed sample of 2000 events, the reconstruction efficiency is $93 \pm 2\%$, and the incidence of substantially erroneous reconstruction less than 1%. The missed or mis-reconstructed events do not constitute a significant bias in any particular region of E_ν , x , or y . The numbers of events thus obtained, in the neutrino energy region $30 < E_\nu < 200$ GeV (where the neutrino energy is defined as the sum of the observed muon and hadron energies), are given in Table 1.

The acceptance in the x and y variables is unity except at large y , where the requirements of five chambers and $E_\mu > 7$ GeV reduce the acceptance. The calculated acceptance is shown in Fig. 6 for several neutrino energies.

The experimental energy resolution and calibration for both the muon and hadron energy measurements can be checked by comparing the observed energy distributions for events which originate in narrow radial annular regions in the apparatus, with Monte Carlo simulations incorporating the neutrino beam characteristics and the presumed energy resolution and calibration. In such regions the energy distribution of kaon neutrinos is reasonably narrow, and comparison of the observed and calculated average and width provides checks on both calibration and resolution. If this is done for events with small y , the bulk of the energy is contributed by the muon, and the comparison checks the muon calibration and resolution.

Conversely, if the comparison is made for high y events, the hadron calorimetry is checked. An example of a comparison is shown in Fig. 7. On the basis of these comparisons we are confident that the calibration and resolution are adequately understood and implemented in the simulation program.

4. TOTAL CROSS-SECTION

The determination of the total cross-section requires a knowledge of the absolute neutrino flux and its energy spectrum. As was seen in Section 2, the narrow-band beam neutrinos originate from decays of particles with well-defined direction and momentum. The neutrino spectrum is therefore determined by decay kinematics and by the beam and detector geometry. The entire neutrino energy range $10 < E_\nu < 200$ GeV is covered in a single exposure. The spectrum has two distinct components. The neutrinos from pion decays are distributed uniformly from 10 to 90 GeV, the kaon neutrinos from 90 to 190 GeV (Fig. 3). The neutrino flux is therefore completely determined by the total beam intensity and the relative amounts of pions and kaons.

The neutrino and antineutrino data have been taken with the same absolute magnet currents in beam and detector magnets. The polarity of the current was chosen such that the muons are focused towards the detector axis. The pion fluxes for the two polarities were about equal. The ratios of kaons to pions were 0.14 ± 0.01 in the positive and 0.046 ± 0.005 in the negative beam. Because of the difference in lifetime and the rising total cross-section, this gives about the same number of interactions from pion and kaon decay in the case of neutrinos, and three times fewer kaon than pion events in the case of antineutrinos.

The total beam intensity has been measured with the beam current transformer installed immediately following the last magnet in the beam line. The transformer output was integrated over every 23 μ sec pulse from the accelerator. The integrated signal was calibrated to +3% on the basis of a test charge applied to a single turn winding through the transformer core.

The beam intensity as measured by the beam current transformer has been compared to the temperature rise observed in the total-absorption calorimeter placed as beam stopper at the end of the decay tunnel. The two measurements agree to within 5%. The relative response of the beam current transformer to a change in beam polarity has been checked against an ion chamber, giving the same result, within 2%, after correction for a change in the specific energy loss of pions and protons. We allow therefore for a $\pm 2\%$ uncertainty in the particle flux ratio of positive and negative beams in addition to the $\pm 3\%$ common uncertainty due to the calibration.

The beam composition has been measured with a differential Čerenkov counter placed at the end of the beam line. This device is a special design utilizing the small beam divergence and giving good separation between pions and kaons by using a very small Čerenkov angle, 1 mrad. Owing to the small Čerenkov angle, very little light is collected per particle. Therefore the signal is integrated over the time of the beam burst.

The particle ratios, independently of beam dispersion, are the ratios of the areas of the particle peaks in an intensity versus pressure curve. The present Čerenkov data have some unforeseen systematic uncertainty in the index of refraction at low pressure, which could affect the integrated pressure curve of the pion peak. We assume therefore a $\pm 10\%$ systematic uncertainty on the π/K ratios as measured by the Čerenkov.

In the negative beam, pions predominate, and the uncertainty in the π^-/K^- ratio does not seriously affect the antineutrino flux from negative pion decay. The muon flux is measured by a $95 \times 95 \text{ cm}^2$ ion chamber after 30 m of iron shielding, and a comparison of the muon flux in the positive and negative beams gives then a strong constraint on the π^+ flux. This constraint has been used to augment the information from the Čerenkov counter.

The various uncertainties in the neutrino flux from pion and kaon decay are included, in Table 2, in the errors of the average slopes of the cross-sections in the relevant energy intervals. They range from $\pm 5\%$ on the π^- flux to $\pm 12\%$ on

the K^- flux, with relatively smaller errors on the flux ratios of antineutrinos and neutrinos, i.e. $\pm 5\%$ on the π^-/π^+ and $\pm 10\%$ on the K^-/K^+ ratios. The uncertainties given in Table 2 have to be applied as over-all scale errors in Figs. 8 and 9. The errors are different and approximately independent for energies below and above 90 GeV.

The energy spectrum is obtained by means of a Monte Carlo calculation which includes the transport of the hadron beams, the decays in the tunnel, the detection geometry, the event-selection criteria, and the contributions of neutrinos from the three-body muon decay of the kaon. The surviving events were attributed weights calculated according to a specific quark parton model in which the antiquark content of the nucleon was given values determined from the analysis of the present experiment as determined in Sections 5 and 6 of this paper.

The total cross-section values were obtained by comparing the energy spectrum of the data with the energy spectrum from the Monte Carlo calculation, obtained as described above and normalized by the flux measurements. The resulting cross-sections are shown in Table 2 and Figs. 8 and 9. Previous results in this energy region [2, 12-14] are shown in Fig. 10 for comparison^{*)}. The errors shown in Figs. 8-10 are statistical only. The scale errors discussed above are omitted. In this experiment, in the energy domain 30-190 GeV, no significant variations in the value of $\sigma_{\text{tot}}/E_\nu$ are observed, in agreement with the scaling hypothesis. However, the result of the Gargamelle collaboration [2] in the energy range 2-5 GeV for the neutrino cross-section slopes are somewhat higher than those found here, and the cross-section ratios $\sigma_{\bar{\nu}}/\sigma_\nu$ are somewhat lower.

In the quark parton model, the difference of the cross-section ratio from one third is due to the antiquark contribution. The experiments indicate that the relative antiquark contribution, $\bar{Q}/(Q+\bar{Q})$, increases from 0.07 ± 0.02 at Gargamelle energies to 0.15 ± 0.02 at the higher energies. This increase must be

^{*)} The cross-section ratio $\sigma_{\bar{\nu}}/\sigma_\nu$ from this experiment has been published previously [15]. Based on the same data, and a better knowledge of the neutrino flux, we obtain now a somewhat higher level of this cross-section ratio. The change is within the systematic flux uncertainties as stated in Ref. 15.

attributed to the combined effect of the onset of charm production near 10 GeV, and to other possible scaling violations.

5. DISTRIBUTIONS IN THE INELASTICITY y

5.1 y -distributions for $30 < E_\nu < 200$ GeV

The observed event numbers for this energy range are shown in Fig. 11. In Fig. 12 these distributions are corrected for acceptance and relative flux. A special cut to remove quasi-elastic scattering has been applied for the purpose of this analysis. Events for which $Q^2 < 1 \text{ GeV}^2$ and $W^2 = M^2 + 2\nu - Q^2 \leq 4 \text{ GeV}^2$ have been removed. The data are fitted with expressions of the form $a + b(1-y)^2$, derived from the quark parton model, expressions (2) and (2'), after integration over x . The fits are clearly satisfactory, and the data are therefore in agreement with this model.

5.2 y -distribution in two energy ranges

In Figs. 13 and 14 the data are shown separately for the energy bins 30-90 GeV and 90-200 GeV, which correspond to neutrinos of pion and kaon origin, respectively. There is no statistically significant difference between the distributions in the two energy ranges.

5.3 Average y values as functions of neutrino energy

In Fig. 15, the average values of y , resolution and acceptance corrected, are shown as function of the neutrino energy. As has already been published [15], no statistically significant variation is observed, in agreement with the predictions of the scaling hypothesis. Averaged over the entire energy range $30 < E_\nu < 200 \text{ GeV}$ we find

$$\langle y \rangle_\nu = 0.49 \pm 0.01$$

$$\langle y \rangle_{\bar{\nu}} = 0.34 \pm 0.01 .$$

5.4 Fraction of quarks in the sea

The effect of scaling violations on the shape of the y -distribution appears to be small. The y -distributions (Fig. 12) are therefore analysed in the framework of the quark parton model, and the effect of scaling violations is estimated

separately, based on the ν -dependence of the integrated structure function as determined in Section 7.

The fits of 5.1 then determine the relative contribution of the antiquark sea. The result from the neutrino y -distribution is:

$$\frac{\int [\bar{q}(x) - \bar{s}(x)] dx}{\int [\bar{q}(x) + q(x)] dx} = \begin{array}{ll} 0.08 \pm 0.04 & \text{no radiative correction} \\ 0.15 \pm 0.04 & \text{with radiative correction [16,17],} \end{array}$$

and from the antineutrino y -distribution it is:

$$\frac{\int [\bar{q}(x) + \bar{s}(x)] dx}{\int [\bar{q}(x) + q(x)] dx} = \begin{array}{ll} 0.16 \pm 0.02 & \text{no radiative correction} \\ 0.15 \pm 0.02 & \text{with radiative correction.} \end{array}$$

Here, and in subsequent applications of the radiative correction, we do not include the uncertainty in this correction in the error, since we do not know how to do this^{*)}. The effect of scaling violations on the antineutrino result is small. The neutrino result, however, might change by an amount which is comparable to the assigned error.

In the quark parton model the antiquark contributions to neutrino and antineutrino scattering differ by twice the strange antiquark distribution. Using the above result we find for the *total* antiquark contribution:

$$\frac{\int \bar{q} dx}{\int (q + \bar{q}) dx} = 0.15 \pm 0.03 .$$

This value is in agreement with the one found on the basis of the total cross-sections, which is independent of radiative corrections. For the *strange* antiquark contribution we find^{**)}

$$\frac{\int \bar{s} dx}{\int (q + \bar{q}) dx} = 0.00 \pm 0.03 .$$

*) The calculation of radiative corrections for neutrino interactions is model-dependent. References 16 and 17 give similar results, although they differ in some detail. The corrections are typically less than 10%, and we assume therefore that the precision of these calculations is adequate to correct the present data.

**) In the foregoing analysis we have dropped the charm quark distributions; they are presumed small, but it may be pointed out that this result is really for the difference $\bar{s}-\bar{c}$ rather than \bar{s} .

The latter result can be compared with the result based on dimuon production in neutrino interactions as interpreted in the GIM model:

$$\frac{\int \bar{s} dx}{\int (q + \bar{q}) dx} = 0.025 \pm 0.01 [18] .$$

A more precise result for the $\bar{q} + \bar{s}$ antiquark constituent can be obtained by noting that at high y , the antineutrino cross-section is dominated by the $\bar{q} + \bar{s}$ antiquark constituency [see expression (6)], and the $(1 - y)^2 q$ contribution can be subtracted using the neutrino data at large y [expression (5)]. In this way we find the result

$$\frac{\int (\bar{q} + \bar{s}) dx}{\int (q + \bar{q}) dx} = 0.16 \pm 0.01 \text{ with radiative correction.}$$

This is our most reliable result for the antiquark fraction; the error is due equally to statistical and flux uncertainties.

5.5 Charge symmetry

If the neutrino interaction is charge symmetric (Section 1.1), then it is expected that at $y = 0$:

$$\left. \frac{d\sigma^{\nu}}{dy} \right|_{y=0} = \left. \frac{d\sigma^{\bar{\nu}}}{dy} \right|_{y=0} .$$

Using the fits of Fig. 12 we find, after a small correction for the neutron excess in iron:

$$\left. \frac{d\sigma^{\bar{\nu}}}{dy} \right|_{y=0} / \left. \frac{d\sigma^{\nu}}{dy} \right|_{y=0} = 1.05 \pm 0.07 , \quad \text{no radiative correction ,}$$

and

$$\left. \frac{d\sigma^{\bar{\nu}}}{dy} \right|_{y=0} / \left. \frac{d\sigma^{\nu}}{dy} \right|_{y=0} = 1.01 \pm 0.07 , \quad \text{radiative correction}$$

The result is in agreement with the expectations of charge symmetry, namely that the integrated F_2 structure function $\int F_2 dx$ is the same for neutrino and anti-neutrino interactions. It has been checked that the effect of scaling violation (see Section 7) does not change this result.

5.6 Scalar cross-section

It is convenient for this discussion to write (1) in terms of three new structure functions $F_L(x)$, $F_R(x)$, and $F_S(x)$ where

$$F_L = 2xF_1 + xF_3$$

$$F_R = 2xF_1 - xF_3$$

and

$$F_S = F_2 - 2xF_1.$$

F_L , F_R , and F_S can be interpreted as the structure functions corresponding to the interaction of left-handed, right-handed, and scalar currents, respectively.

In the naive quark parton model $F_S = 0$, $F_L = 2q$, and $F_R = 2\bar{q}$. In terms of the new structure functions:

$$\frac{d^2\sigma^V}{dx dy} = \frac{G^2 ME_V}{2\pi} [F_L + F_R(1-y)^2 + 2F_S(1-y)] \quad (1a)$$

$$\frac{d^2\sigma^{\bar{V}}}{dx dy} = \frac{G^2 ME_V}{2\pi} [F_L(1-y)^2 + F_R + 2F_S(1-y)]. \quad (1b)$$

The quantity $\int 2F_S dx / \int (F_L + F_R) dx = \int F_S dx / \int 2xF_1 dx$ corresponds to the ratio R of longitudinal to transverse cross-section in electron inclusive scattering in the limit $Q^2 \gg M^2$.

As already noted, the experimental results are consistent with $F_S = 0$, that is, without a term in $(1-y)$ and consequent violation of the naive quark parton model. We have also fitted the data to the more complete expressions (1a) and (1b). The results have to be corrected for radiative corrections, charge symmetry violations due to the strange sea, and the Q^2 dependence of the structure functions. The latter corrections are based on the data presented in Section 7 and their QCD fits, and take account of the fact that the data at larger y correspond to larger Q^2 than those at smaller y , and that the structure functions change somewhat in that interval of Q^2 . The dominant term F_L decreases with $\ln Q^2$ while the smaller term F_R increases with $\ln Q^2$. The net effect simulates a small F_S term which must be subtracted. We find

$$\begin{aligned}
 R = \frac{\int F_S dx}{\int 2xF_1 dx} &= -0.02 \pm 0.03 && \text{uncorrected} \\
 &= -0.05 \pm 0.03 && \text{with strange sea } \bar{s} = 1/5 \bar{q} \\
 &= +0.03 \pm 0.03 && \text{after radiative correction} \\
 &= -0.03 \pm 0.04 && \text{after correction for } Q^2 \text{ dependence} \\
 &&& \text{of structure function .}
 \end{aligned}$$

There is clearly no evidence for a non-zero F_S term, and, leaving some room for underestimate of the uncertainty, we believe an uncertainty of about 0.05 for $\int F_S dx / \int 2xF_1 dx$ can be put. The results obtained from inelastic electron scattering experiments at lower Q^2 have been considerably higher [19] but with rather larger uncertainty. In view also of recent changes in the measured values [19] perhaps it is too early to be certain that the difference between the neutrino and electron scattering results in R is significant.

6. STRUCTURE FUNCTIONS

6.1 Structure functions averaged in the neutrino energy range $30 < E_\nu < 200$ GeV

In Fig. 16 the event distributions in x for neutrino and antineutrino interactions in the neutrino energy range $30 < E_\nu < 200$ GeV are shown, divided into several y bins. The results of a fit to the naive quark parton model, expressions (2) and (2'), are also shown. It is clearly not difficult to reproduce the experimental result in terms of just two structure functions, as expected in this model. At small y , neutrino and antineutrino x distributions are alike, both equal to $q(x) + \bar{q}(x) = F_2(x)$ in the model, while at large y they are very different: the neutrino x distribution is broad, and the antineutrino x distribution is narrow, as in the model $q(x)$ and $\bar{q}(x)$, respectively.

Continuing in the frame of the quark parton model, we find the total quark structure function $F_2(x) = q(x) + \bar{q}(x)$ and the valence quark structure function $xF_3(x) = q(x) - \bar{q}(x)$ in terms of the sum and difference of the neutrino cross-sections according to the expressions:

$$\begin{aligned}
 q(x) + \bar{q}(x) = F_2(x) &= \frac{\pi}{G^2 M E_\nu} \left[\frac{d^2 \sigma^V}{dx dy} + \frac{d^2 \sigma^{\bar{V}}}{dx dy} \right] \left[1 + (1-y)^2 \right] - \\
 &\quad - \left[2s(x) + \delta \left(q(x) - \bar{q}(x) \right) \right] \left[\frac{1 - (1-y)^2}{1 + (1-y)^2} \right] \quad (11)
 \end{aligned}$$

and

$$q(x) - \bar{q}(x) = xF_3(x) = \frac{\pi}{G^2 ME_\nu} \left[\frac{d^2 \sigma^\nu}{dx dy} - \frac{d^2 \sigma^{\bar{\nu}}}{dx dy} \right] \left[1 - (1-y)^2 \right] - \delta [q(x) - \bar{q}(x)] \left[\frac{1 + (1-y)^2}{1 - (1-y)^2} \right]. \quad (12)$$

The terms in δ are the corrections for the neutron excess in iron.

$$\delta = \frac{2N - A}{3A} = 0.023.$$

The distribution $s(x)$ enters in the determination of $F_2(x)$ as a correction which can be as much as $\sim 20\%$ at very small x , but is generally a few per cent. In agreement with the results from antineutrino dimuon production [18], we have taken $s(x) = 1/5 \bar{q}(x)$.

The antiquark structure function is best determined from the antineutrino cross-section at large y , which gives directly $\bar{q}(x) + \bar{s}(x)$, after subtraction of the $q(x)$ background on the basis of the neutrino cross-sections at high y :

$$\bar{q}(x) + \bar{s}(x) = \frac{\pi}{G^2 ME_\nu} \left[\frac{d^2 \sigma^{\bar{\nu}}}{dx dy} - (1-y)^2 \frac{d^2 \sigma^\nu}{dx dy} \right]_{y \rightarrow 1}. \quad (13)$$

In the structure function determination, the absolute neutrino and antineutrino fluxes enter as a common scale factor. The same is approximately true for the reconstruction efficiency. The relative neutrino and antineutrino fluxes have an uncertainty of approximately 5%. The three effects give a total scale error of $\pm 6\%$ for $F_2(x)$ and $\pm 8\%$ for $xF_3(x)$. The relative flux of neutrinos from π and K decay, which is experimentally known to 10% only, is not a problem, since there is an overlapping region in x and Q^2 for pion and kaon neutrinos, and the relative flux is internally monitored with $\pm 2\%$ accuracy.

The acceptance corrections are reliably calculated by a Monte Carlo simulation and are generally small. The F_2 structure function has been determined using all the data. In order to limit the uncertainties due to a large subtraction, xF_3 has been determined using the data with $y > 0.2$, and the antiquark distribution using data with $y > 0.5$ only.

The main problem of the analysis is the correction for measurement errors (unsmearing corrections), which are large at large x where the structure functions vary rapidly with x . We proceed by assuming a "true" structure function and calculate by Monte Carlo simulation, on the basis of the known experimental resolution functions, the result to be expected in the apparatus. By iteration a "true" distribution which reproduces the experimental result is found. The "unsmearing factor" is the ratio of Monte Carlo events for any particular (x, Q^2) bin in the "true" distribution divided by those in the resolution smeared distribution. If this factor differs from unity by more than 30%, the bin is not retained. In this way the bins in $F_2(x)$ and $xF_3(x)$ with $x > 0.7$ have been lost.

The results for the structure functions $q(x) + \bar{q}(x)$, $q(x) - \bar{q}(x)$ and $\bar{q}(x) + \bar{s}(x)$, determined for all data with neutrino energy between 30 and 200 GeV, corrected for resolution and acceptance, are shown in Figs. 17 and 18.

These distributions have been fitted to simple analytical expressions:

$$q(x) - \bar{q}(x) \propto \sqrt{x}(1-x)^n$$

$$\bar{q}(x) + \bar{s}(x) \propto (1-x)^m.$$

Good fits are obtained with $n = 3.5 \pm 0.5$ and $m = 6.5 \pm 0.5$.

At present there is no theory for these structure functions. The observed distributions are, however, not in disagreement with theoretical prejudices, such as, that xF_3 should go to zero as x goes to zero, and the observed values for m and n are similar to those which have been suggested by "counting rules" [20].

6.2 Comparison of total antiquark and strange antiquark distributions

Neutrino interactions in which two muons of opposite sign are observed can be shown to be due to the production and subsequent decay of charmed particles. Furthermore, the dynamics of the process are in agreement with the predictions of the GIM current [21].

The GIM model predicts further that $\sim 95\%$ of charm production by antineutrinos is on the strange antiquark component of the nucleon. The structure function measured in opposite sign dimuon production by antineutrinos is then a direct measure of the strange sea. Unfortunately, the dimuon data are limited to only

55 events. In Fig. 19 we compare the two sea structure functions, that for the $\bar{q} + \bar{s}$ sea as seen in antineutrino charged current reactions at high y and that for the \bar{s} sea as discussed above. Both are uncorrected for acceptance and resolution. The two sea distributions have the same shape, within experimental uncertainty. In the quark parton model this may be understood as a reflection of similar masses of up-down and strange quarks.

6.3 Fraction of nucleon momentum carried by quarks

In the quark parton model, the integral of $F_2(x)$ is a measure of the fraction of the nucleon momentum carried by quarks. We find

$$\int F_2(x) dx = 0.44 \pm 0.02, \quad 30 < E_\nu < 90 \text{ GeV}$$

and

$$\int F_2(x) dx = 0.45 \pm 0.03, \quad 90 < E_\nu < 200 \text{ GeV}.$$

In the frame of this model, the remainder, or approximately one half the nucleon momentum, is then carried by gluons.

6.4 Comparison of neutrino and charged lepton structure functions

In the quark parton model (Section 1.3) the structure functions observed in electron or muon inelastic scattering, and the $F_2(x)$ structure function observed in neutrino scattering, are related by expression (10). In Fig. 20 the distribution obtained in the SLAC electron-deuteron scattering experiments [22] is compared with our results in the E_ν range $20 < E_\nu < 30$ GeV, which correspond in Q^2 approximately to the SLAC regime. The agreement between the two different measurements of F_2 is remarkable.

6.5 Total number of valence quarks in the nucleon

In the introduction we have noted that in the quark parton model, $\int_0^1 F_3(x) dx$ represents the total number of valence quarks in the nucleon [6] and is therefore expected to be three. Experimentally, the more directly measured quantity is $xF_3(x)$ which, except for small corrections, is obtained directly from the difference of neutrino and antineutrino cross-sections. To get $\int F_3(x) dx$, it is necessary to divide by x , which presents a problem at small x . In Fig. 21 we show the integral $\int_{x_0}^1 F_3(x) dx$ as function of the cut-off x_0 at small x . As a

result of the $1/x$ weighting, the error in $\int_{x_0}^1 F_3(x) dx$ becomes large as $x_0 \rightarrow 0$. We choose $x_0 = 5 \times 10^{-3}$ with $\int_{5 \times 10^{-3}}^1 F_3(x) dx = 2.7 \pm 0.3$ (including flux uncertainties) and extrapolate following the analytical fit to find

$$\int_0^1 F_3(x) dx = 3.2 \pm 0.5 ,$$

where the error has been enlarged to make some allowance for the uncertainty in the extrapolation. The agreement with the expectation of the quark parton model is good. We have verified that this conclusion is not affected by the scale breaking observed for xF_3 (see Section 7). A calculation based on the parametrization of Ref. 23 and the QCD fit of Section 7.2 gives a value of 2.5 for the integral $\int_{x_0}^1 F_3(x) dx$ for three valence quarks and $x_0 = 5 \times 10^{-3}$, very close to the value obtained from the analytic fit according to Fig. 21.

7. STRUCTURE FUNCTIONS AND SCALE BREAKING

7.1 Experimental results

The structure functions are functions of two variables, which are taken to be $x = Q^2/2\nu$, and either Q^2 or $\nu = p \cdot q = ME_h$. If scaling is valid, the structure functions are independent of Q^2 or ν , so that these variables characterize the deviations from scaling. Theoretically the Q^2 dependence is sometimes more immediately calculable than the ν dependence; however, the analysis in terms of ν or equivalently E_h offers two advantages: for given E_h the shape of the structure function is independent of flux uncertainties, and for given E_h the entire x distribution is measured. For fixed Q^2 , knowledge of the neutrino flux is essential to the measurement of the shape of the structure functions, and the structure function is measured only in a limited domain in x . The domain in x and Q^2 reasonably explored in this experiment is shown in Fig. 22. Also shown are those reported in electron-deuteron [22,24] and muon-deuteron [25] scattering experiments.

In Table 3 we give our results for f_2 and xF_3 in x and E_h bins. In order to convert E_h to Q^2 it is only necessary to remember that $Q^2 = 2xME_h$, and to add the over-all error due to the beam uncertainties described in Section 6.2.

The data of Table 3 are shown graphically in Fig. 23. In Figs. 24 and 25 they are shown as functions of Q^2 .

In Fig. 26 we give the results for the integrals $\int_0^1 F_2(x, E_h) dx$ and $\int_0^1 xF_3(x, E_h) dx$, and in Fig. 27 the result for the average widths,

$$\int_0^1 xF_2(x, E_h) dx \bigg/ \int_0^1 F_2(x, E_h) dx \quad \text{and} \quad \int_0^1 x^2 F_3(x, E_h) dx \bigg/ \int_0^1 xF_3(x, E_h) dx ,$$

of F_2 and xF_3 as functions of E_h . We complete the presentation of the experimental results with the E_h dependence of the antiquark fraction

$$\frac{\int [\bar{q}(x) + \bar{s}(x)] dx}{\int [q(x) + \bar{q}(x)] dx} ,$$

and the antiquark width

$$\int_0^1 x[\bar{q}(x) + \bar{s}(x)] dx \bigg/ \int_0^1 [\bar{q}(x) + \bar{s}(x)] dx$$

in Fig. 28.

The function which is most precisely measured, $F_2(x)$, shows clear scaling violation and, qualitatively, the shrinking towards small x expected in QCD. The shrinkage is dramatic when results at very different energies are compared. In Fig. 29 the Gargamelle results [26], the SLAC electron scattering results [22], as well as the results of this experiment are reproduced. Scaling violations in the other structure functions are almost hidden by the experimental errors.

7.2 QCD fit to the data

The data points of Table 3 on F_2 and xF_3 have been used to perform a parametrized QCD fit following the procedure of Buras and Gaemers [23]. The valence quarks are parametrized $xF_3(x, Q^2) \propto x^{\eta_1(s)} (1-x)^{\eta_2(s)}$ where η_1 and η_2 depend linearly on $s = \ln [\ln (Q^2/\Lambda^2)/\ln (Q_0^2/\Lambda^2)]$. It has been demonstrated [23] that such an ansatz satisfies the QCD moment relations to very high accuracy. For the development of the sea quarks with Q^2 , the method is approximate, using a parametrization $\bar{q}(x, Q^2) = A(s)(1-x)^{B(s)}$, where A and B are determined by using the QCD equations for the second and third moments of F_2 only. This procedure is

approximately valid for a narrow sea distribution and also allows the determination of the width of the gluon distribution.

This QCD fit gives a surprisingly good description of our data over the Q^2 range $3 < Q^2 < 200 \text{ GeV}/c^2$ which has been used as input, as well as the electron scattering data [22] which has not been used in the input. The charmed sea has been put zero at $Q^2 = 1.8 \text{ GeV}/c^2$. The best fit parameters are:

$$\Lambda = 0.47 \pm 0.1 (\pm 0.1 \text{ systematic errors}) \text{ GeV}$$

$$\left. \begin{aligned} \eta_1(s) &= 0.56 - 0.92 \times s \times 4/25 \\ \eta_2(s) &= 2.71 + 5.08 \times s \times 4/25 \end{aligned} \right\} \text{ for } Q_0^2 = 5 \text{ GeV}/c^2 .$$

Independent of QCD, this parametrization of the valence quark distribution may be regarded as a good description of F_2 at large x and of xF_3 at all x . The results of the fit are shown in Figs. 25 to 27 and in Fig. 30. No fits are shown for the E_h variation of $\int F_2(x) dx$, and the amount and width of the sea, because these results depend particularly strongly on small Q^2 , where the method of Buras and Gaemers may not be sufficiently reliable.

8. CONCLUSIONS

We list here the more important results of this experiment:

- a) The neutrino and antineutrino total cross-sections show no statistically significant deviation from proportionality to E_ν .
- b) No deviation from the Callan-Gross relation is observed, in agreement with the quark parton model.
- c) The amount of $\bar{q} + \bar{s}$ sea relative to the total momentum carried by quarks is 0.16 ± 0.01 .
- d) For comparable Q^2 , the shapes of the F_2 structure function observed in this experiment is closely similar to that observed in electron-deuteron scattering, in agreement with the quark parton model.
- e) The magnitude of the F_2 structure function is compatible with that observed in electron scattering, after allowance for the ratio of the square of the weak and electromagnetic coupling strengths, in agreement with the quark parton model.

f) Clear scaling violations are observed in the F_2 structure function. The Q^2 dependences of F_2 and xF_3 are in good agreement with QCD predictions.

REFERENCES

- [1] G. Miller et al., Phys. Rev. D 5 (1972) 528.
- [2] T. Eichten et al., Phys. Letters 46B (1973) 274.
- [3] J.D. Bjorken, Phys. Rev. 179 (1969) 1547.
- [4] J.D. Bjorken and E.A. Paschos, Phys. Rev. 185 (1969) 1975.
- [5] C.G. Callan and D.J. Gross, Phys. Rev. Letters 22 (1969) 156.
- [6] D.J. Gross and C.H. Llewellyn Smith, Nuclear Phys. B14 (1969) 337.
- [7] For ep, ed:
 - E.M. Riordan et al., SLAC Pub. 1634 (1975).
 - W.E. Atwood, SLAC Pub. 185 (1975).
 - R.E. Taylor, Proc. Symposium on Lepton and Photon Interactions at High Energies, Stanford, 1975.
- For μ Fe:
 - D. Fox et al., Phys. Rev. Letters 33 (1974) 1504.
 - Y. Watanabe et al., Phys. Rev. Letters 35 (1975) 898.
 - C. Chang et al., Phys. Rev. Letters 35 (1975) 901.
- For μ p, μ d:
 - H.L. Anderson et al., Phys. Rev. Letters 37 (1976) 4.
 - H.L. Anderson et al., Phys. Rev. Letters 38 (1977) 1450.
- For ν :
 - P.C. Bosetti et al., to be published in Nuclear Physics.
- [8] G. Cavallari et al., Proc. Nuclear Science Symposium, San Francisco, 1977.
- [9] G. Marel et al., Nuclear Instrum. Methods 141 (1977) 43.
- [10] M. Holder et al., Nuclear Instrum. Methods 148 (1978) 235.
- [11] M. Holder et al., Nuclear Instrum. Methods 151 (1978) 69.
- [12] P.C. Bosetti et al., Phys. Letters 70B (1977) 273.
- [13] B.C. Barish et al., Phys. Rev. Letters 39 (1977) 741.
- [14] A.E. Astratyan et al., Phys. Letters B76 (1978) 239.
- [15] M. Holder et al., Phys. Rev. Letters 39 (1977) 433.

- [16] J. Kiskis, Phys. Rev. D 8 (1973) 2129.
R. Barlow and S. Wolfram, Oxford report OUNP 24/78 (1978).
- [17] A. de Rújula, R. Petronzio and A. Savoy-Navarro, to be published.
- [18] M. Holder et al., Phys. Letters 69B (1977) 377. The result quoted here differs slightly from that of the original letter, because of the new determination of the total cross-section ratio $\sigma_{\bar{\nu}}/\sigma_{\nu}$ of the present paper.
- [19] The most recent value of $R = 0.21 \pm 0.1$ is given by M. Mestayer, SLAC report 214 (1978) from a combination of data as an average over the kinematic range $3 < Q^2 < 18 \text{ GeV}^2$.
- [20] S.J. Brodsky and G. Farrar, Phys. Rev. Letters 31 (1973) 1153 and Phys. Rev. D 11 (1975) 1309.
V.A. Matveev, R.M. Muradyan and A.N. Tavkhelidze, Nuovo Cimento Letters 7 (1973) 719.
- [21] S.L. Glashow, J. Iliopoulos and L. Maiani, Phys. Rev. D 2 (1970) 1285.
- [22] E.M. Riordan et al., SLAC Pub. 1634 (1975).
- [23] A.J. Buras and K.J.F. Gaemers, Nuclear Phys. B132 (1978) 249.
- [24] J.T. Friedman and H.W. Kendall, Annu. Rev. Nuclear Sci. 22 (1972) 203.
- [25] H.L. Anderson et al., Phys. Rev. Letters 37 (1976) 4.
- [26] H. Deden et al., Nuclear Phys. B85 (1975) 269.

Table 1

Observed numbers of events

Neutrino	23,140
Antineutrino	6,207

Table 2

Total cross-section slopes for neutrinos and anti-neutrinos [from pions (< 90 GeV), kaons (> 90 GeV), and their average] and the corresponding total cross-section ratios

E_ν (GeV)	σ_ν/E_ν ($\times 10^{-38}$ cm ² /GeV)	$\sigma_{\bar{\nu}}/E_\nu$	$\sigma_{\bar{\nu}}/\sigma_\nu$
30-90	0.62 ± 0.04	0.30 ± 0.02	0.48 ± 0.025
90-190	0.63 ± 0.05	0.31 ± 0.04	0.49 ± 0.05
30-190	0.62 ± 0.03	0.30 ± 0.02	0.48 ± 0.02

Table 3

Structure functions F_2 and xF_3 in bins of x and E_h . Statistical and systematic errors are indicated. The "unsmearing correction" is the factor which has been applied to account for the resolution of the apparatus. All data points have a scale error in common which is $\pm 6\%$ for F_2 and $\pm 8\%$ for xF_3 .

E_h (GeV)	x	Q^2 (GeV) ²	$F_2 \pm \sigma \pm \sigma_{\text{system}}$	Unsmearing correction	$xF_3 \pm \sigma$
5 to 10	0.06-0.1	1.126	$1.03 \pm 0.10 \pm 0.03$	1.034	
	0.1-0.2	2.11	$1.14 \pm 0.07 \pm 0.05$	1.188	
	0.2-0.3	3.52	$0.95 \pm 0.06 \pm 0.05$	1.283	
	0.3-0.4	4.92	$0.76 \pm 0.06 \pm 0.05$	1.36	
	0.4-0.5	6.33	$0.52 \pm 0.05 \pm 0.04$	1.29	
	0.5-0.6	7.74	$0.30 \pm 0.04 \pm 0.03$	1.185	
	0.6-0.7				
10 to 20	0.03-0.06	1.27	$0.99 \pm 0.08 \pm 0.05$	0.936	
	0.06-0.1	2.25	$1.13 \pm 0.07 \pm 0.04$	0.95	0.73 ± 0.25
	0.1-0.2	4.22	$1.10 \pm 0.05 \pm 0.03$	0.95	0.75 ± 0.15
	0.2-0.3	7.04	$0.91 \pm 0.05 \pm 0.03$	0.99	0.80 ± 0.14
	0.3-0.4	9.85	$0.61 \pm 0.04 \pm 0.03$	1.07	0.63 ± 0.13
	0.4-0.5	12.66	$0.39 \pm 0.03 \pm 0.02$	1.08	0.42 ± 0.09
	0.5-0.6	15.48	$0.26 \pm 0.025 \pm 0.02$	1.12	0.33 ± 0.08
20 to 30	0.03-0.06	2.11	$1.16 \pm 0.09 \pm 0.05$	0.93	
	0.06-0.1	3.75	$1.20 \pm 0.07 \pm 0.05$	0.95	0.56 ± 0.16
	0.1-0.2	7.04	$1.10 \pm 0.05 \pm 0.03$	1.00	0.80 ± 0.10
	0.2-0.3	11.72	$0.854 \pm 0.045 \pm 0.03$	1.08	0.80 ± 0.09
	0.3-0.4	16.4	$0.55 \pm 0.04 \pm 0.03$	1.14	0.60 ± 0.07
	0.4-0.5	21.1	$0.33 \pm 0.025 \pm 0.03$	1.16	0.24 ± 0.05
	0.5-0.6	25.8	$0.20 \pm 0.02 \pm 0.03$	1.16	0.21 ± 0.04
	0.6-0.7	30.5	$0.107 \pm 0.015 \pm 0.02$	0.99	0.108 ± 0.03
30 to 50	0-0.03	1.126	$1.00 \pm 0.10 \pm 0.07$	0.92	
	0.03-0.06	3.38	$1.29 \pm 0.08 \pm 0.05$	0.97	0.50 ± 0.13
	0.06-0.1	6.00	$1.20 \pm 0.06 \pm 0.03$	0.99	0.61 ± 0.10
	0.1-0.2	11.26	$1.10 \pm 0.04 \pm 0.03$	0.99	0.69 ± 0.07
	0.2-0.3	11.76	$0.84 \pm 0.04 \pm 0.03$	1.06	0.75 ± 0.06
	0.3-0.4	26.26	$0.53 \pm 0.03 \pm 0.02$	1.06	0.55 ± 0.05
	0.4-0.5	33.77	$0.34 \pm 0.02 \pm 0.02$	1.11	0.35 ± 0.04
	0.5-0.6	41.27	$0.20 \pm 0.02 \pm 0.02$	1.12	0.19 ± 0.03
	0.6-0.7	48.78	$0.084 \pm 0.010 \pm 0.02$	1.00	0.075 ± 0.017

Table 3 (cont'd)

E_h (GeV)	x	Q^2 (GeV) ²	$F_2 \pm \sigma \pm \sigma_{\text{system}}$	Unsmearing correction	$xF_3 \pm \sigma$
50 to 75	0 -0.03	1.76	$1.32 \pm 0.12 \pm 0.06$	0.88	
	0.03-0.06	5.28	$1.51 \pm 0.10 \pm 0.04$	0.96	0.50 ± 0.15
	0.06-0.1	9.38	$1.45 \pm 0.09 \pm 0.03$	0.94	0.57 ± 0.12
	0.1 -0.2	17.59	$1.12 \pm 0.05 \pm 0.02$	1.02	0.86 ± 0.07
	0.2 -0.3	29.31	$0.82 \pm 0.04 \pm 0.02$	1.08	0.705 ± 0.06
	0.3 -0.4	41.04	$0.53 \pm 0.03 \pm 0.02$	1.05	0.50 ± 0.05
	0.4 -0.5	52.76	$0.36 \pm 0.03 \pm 0.02$	1.15	0.33 ± 0.04
	0.5 -0.6	64.49	$0.17 \pm 0.02 \pm 0.02$	1.09	0.184 ± 0.025
	0.6 -0.7	76.21	$0.07 \pm 0.01 \pm 0.015$	1.05	0.08 ± 0.02
75 to 100	0 -0.03	2.46	$1.23 \pm 0.11 \pm 0.04$	0.97	0.53 ± 0.16
	0.03-0.06	7.39	$1.42 \pm 0.12 \pm 0.03$	0.94	0.67 ± 0.15
	0.06-0.1	13.13	$1.28 \pm 0.09 \pm 0.03$	0.95	0.64 ± 0.13
	0.1 -0.2	24.62	$1.06 \pm 0.05 \pm 0.03$	0.98	0.80 ± 0.07
	0.2 -0.3	41.04	$0.80 \pm 0.05 \pm 0.02$	1.03	0.66 ± 0.06
	0.3 -0.4	57.45	$0.58 \pm 0.04 \pm 0.02$	1.11	0.50 ± 0.05
	0.4 -0.5	73.87	$0.31 \pm 0.03 \pm 0.03$	1.14	0.26 ± 0.04
	0.5 -0.6	90.28	$0.16 \pm 0.02 \pm 0.03$	1.22	0.15 ± 0.03
	0.6 -0.7	106.70	$0.077 \pm 0.014 \pm 0.015$	1.07	0.075 ± 0.025
100 to 150	0 -0.03	3.52	$1.15 \pm 0.10 \pm 0.06$	0.94	0.52 ± 0.13
	0.03-0.06	10.55	$1.50 \pm 0.12 \pm 0.06$	1.04	0.56 ± 0.13
	0.06-0.1	18.76	$1.50 \pm 0.10 \pm 0.06$	1.05	0.62 ± 0.13
	0.1 -0.2	35.17	$1.10 \pm 0.05 \pm 0.03$	1.02	0.76 ± 0.06
	0.2 -0.3	58.63	$0.76 \pm 0.04 \pm 0.03$	1.02	0.63 ± 0.05
	0.3 -0.4	82.07	$0.56 \pm 0.035 \pm 0.03$	1.10	0.51 ± 0.04
	0.4 -0.5	105.52	$0.27 \pm 0.022 \pm 0.02$	1.13	0.30 ± 0.025
	0.5 -0.6	129.0	$0.154 \pm 0.016 \pm 0.02$	1.14	0.15 ± 0.02
	0.6 -0.7	152.4	$0.092 \pm 0.014 \pm 0.02$	1.12	0.09 ± 0.016
150 to 200	0.1 -0.2	49.25	$1.24 \pm 0.11 \pm 0.04$	0.97	
	0.2 -0.3	82.07	$0.84 \pm 0.09 \pm 0.04$	0.87	
	0.3 -0.4	114.9	$0.57 \pm 0.08 \pm 0.04$	0.92	
	0.4 -0.5	147.7	$0.22 \pm 0.05 \pm 0.04$	1.00	
	0.5 -0.6	180.6	$0.14 \pm 0.03 \pm 0.04$	1.12	

Figure captions

- Fig. 1 : Diagram illustrating the inclusive neutrino scattering process.
- Fig. 2 : Scatter plot of measured neutrino energy (muon + hadron energy) versus detector radius for a sample of events. The separate bands are due to neutrinos from pion and kaon decay.
- Fig. 3 : Neutrino and antineutrino energy spectra, integrated over the fiducial area of the detector.
- Fig. 4 : Over-all view of detector.
- Fig. 5 : Dimension of central region which is excluded from fiducial volume.
- Fig. 6 : Acceptance of the apparatus as function of the scaling variable y .
- Fig. 7 : Observed and simulated energy distributions in a restricted interval of impact radius. This comparison checks the calibration and resolution of the measurements (see text).
- Fig. 8 : Neutrino and antineutrino total cross-sections as a function of the neutrino energy.
- Fig. 9 : Ratio of antineutrino to neutrino total cross-sections as a function of the neutrino energy.
- Fig. 10 : Comparison of the results of this experiment for the total cross-section with previous results.
- Fig. 11 : Observed numbers of events as a function of y , for measured neutrino energy between 30 and 200 GeV.
- Fig. 12 : Distributions in y for neutrinos and antineutrinos, after corrections for acceptance, resolution and flux.
- Fig. 13 : Corrected y distributions for pion neutrinos, $30 < E_\nu < 90$ GeV.
- Fig. 14 : Corrected y distributions for kaon neutrinos, $90 < E_\nu < 200$ GeV.
- Fig. 15 : Average value of y as a function of neutrino energy.

- Fig. 16 : Event distributions in x for several bins in y .
- Fig. 17 : $F_2(x)$ and $xF_3(x)$ averaged over the data $30 < E_\nu < 200$ GeV.
- Fig. 18 : The antiquark structure function $\bar{q}(x) + \bar{s}(x)$ averaged over the data $30 < E_\nu < 200$ GeV and normalized to $\int [q(x) + \bar{q}(x)] dx = 1$.
- Fig. 19 : The nucleon antiquark component $\bar{q} + \bar{s}$ as seen in antineutrino scattering at large y , compared to the strange component \bar{s} as seen in antineutrino dimuon (charm) production. Both distributions are raw data uncorrected for resolution or acceptance.
- Fig. 20 : Comparison of F_2 structure function observed in electron-deuteron scattering with F_2 as seen in neutrino scattering in the same momentum transfer region. The two distributions have been normalized to the same area.
- Fig. 21 : $\int_{x_0}^1 xF_3(x) dx/x$ versus x_0 . The solid line is drawn on the basis of three valence quarks and the analytical fit to $xF_3(x) \sim \sqrt{x}(1-x)^{3.5}$ of Section 6.1.
- Fig. 22 : Domain in x and Q^2 for which structure functions are reported here, as well as corresponding domains for electron (Ref. 22) and muon (Ref. 25) scattering.
- Fig. 23 : $F_2(x)$ and $xF_3(x)$ for different ranges of the hadron energy. The solid and dotted lines represent fits to the data in the frame of the QCD theory.
- Fig. 24 : $F_2(x)$ in different x bins as a function of $\ln Q^2$.
- Fig. 25 : $xF_3(x)$ in different x bins as a function of $\ln Q^2$.
- Fig. 26 : $\int_0^1 F_2(x) dx$ and $\int_0^1 xF_3(x) dx$ versus E_h . The curve is the QCD fit discussed in the text.
- Fig. 27 : The average widths $\bar{x}_{F_2} = \int_0^1 xF_2(x) dx / \int_0^1 F_2(x) dx$ and $\bar{x}_{F_3} = \int_0^1 x^2F_3(x) dx / \int_0^1 xF_3(x) dx$ versus E_h . The curves are the QCD fits discussed in the text.

Fig. 28 : Antiquark fraction $\int_0^1 [\bar{q}(x) + \bar{s}(x)] dx / \int_0^1 [q(x) + \bar{q}(x)] dx$ and width of antiquark distribution $\int_0^1 x[\bar{q}(x) + \bar{s}(x)] dx / \int_0^1 [\bar{q}(x) + \bar{s}(x)] dx$ versus E_h .

Fig. 29 : Comparison of F_2 structure function seen in different lepton energy domains. The Gargamelle data are from Ref. 26 and the electron-deuteron data from Ref. 22.

Fig. 30 : Comparison of the F_2 structure function as obtained by this experiment with data from ed scattering (open points, Ref. 22) and a fit based on the QCD parametrization of Ref. 23.

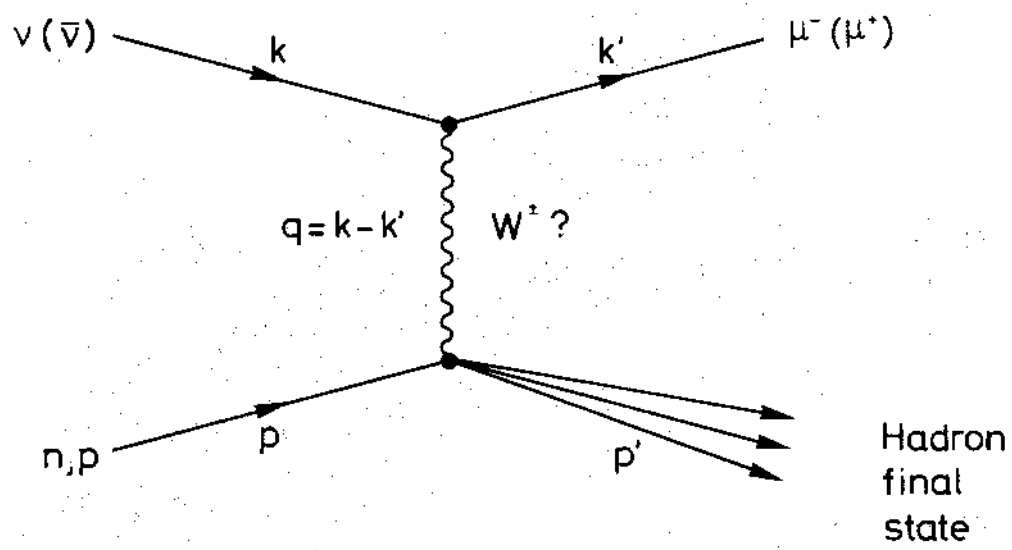


Fig. 1

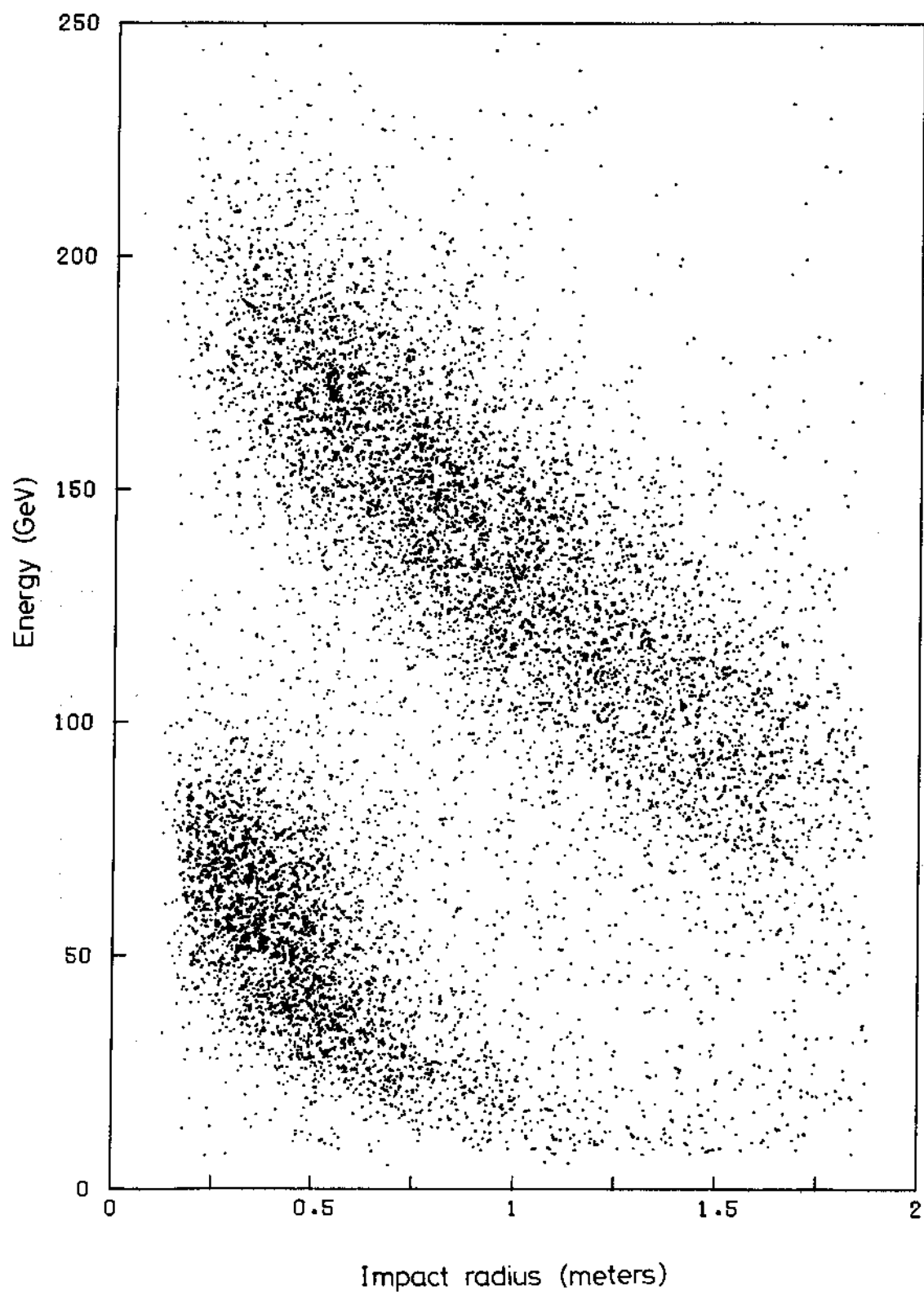


Fig. 2

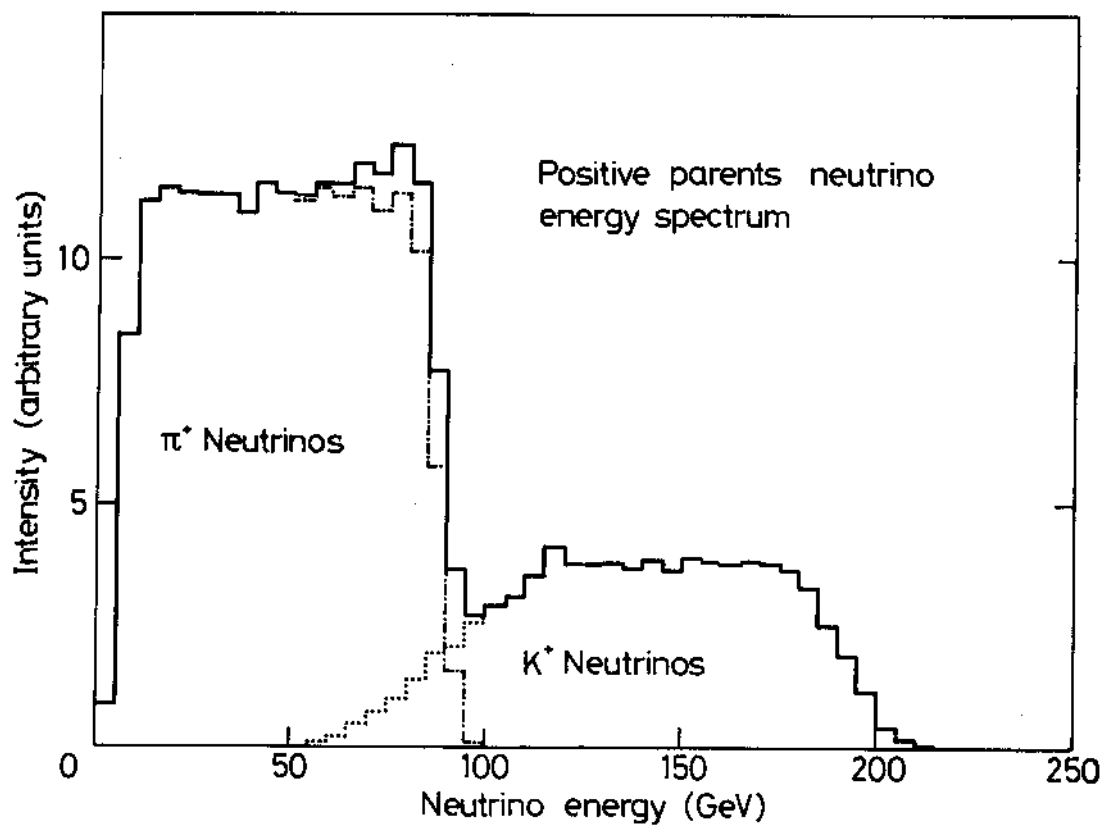
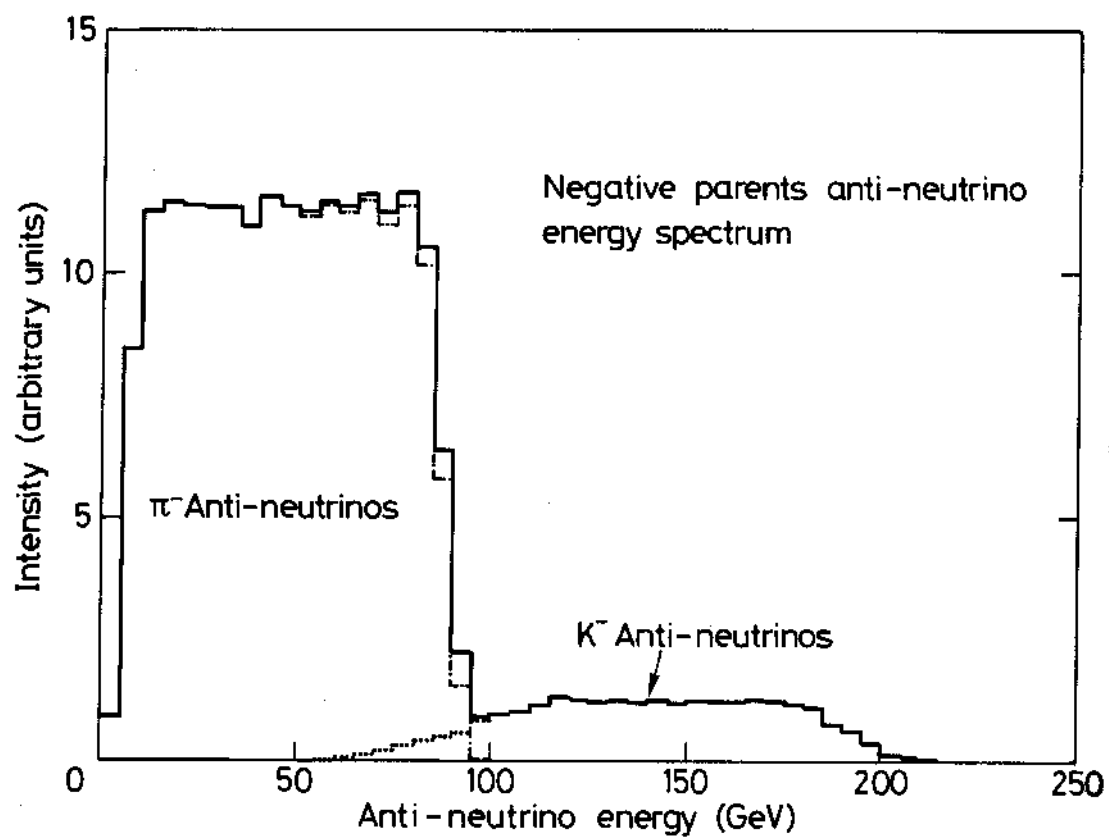


Fig. 3

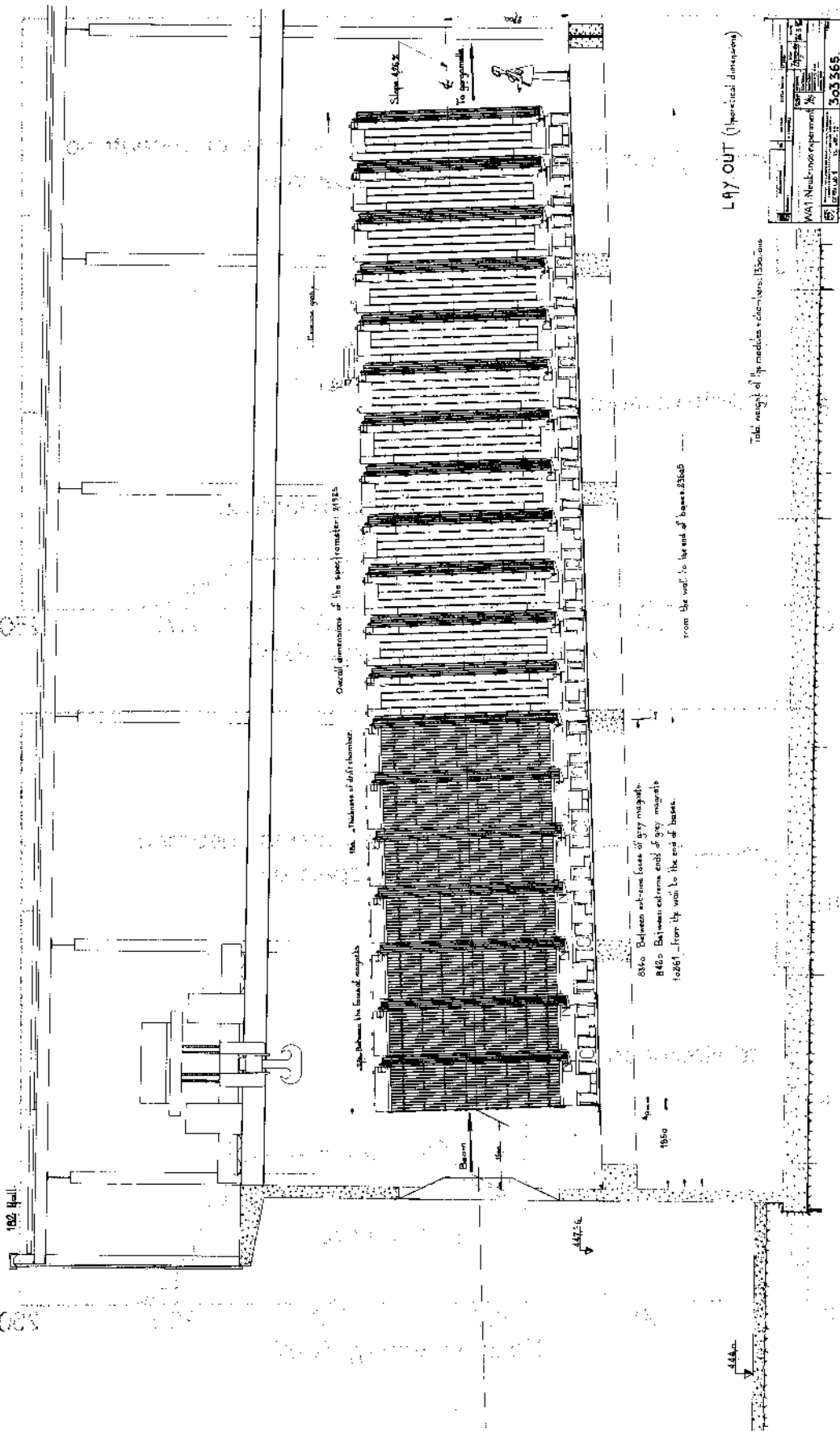


Fig. 4

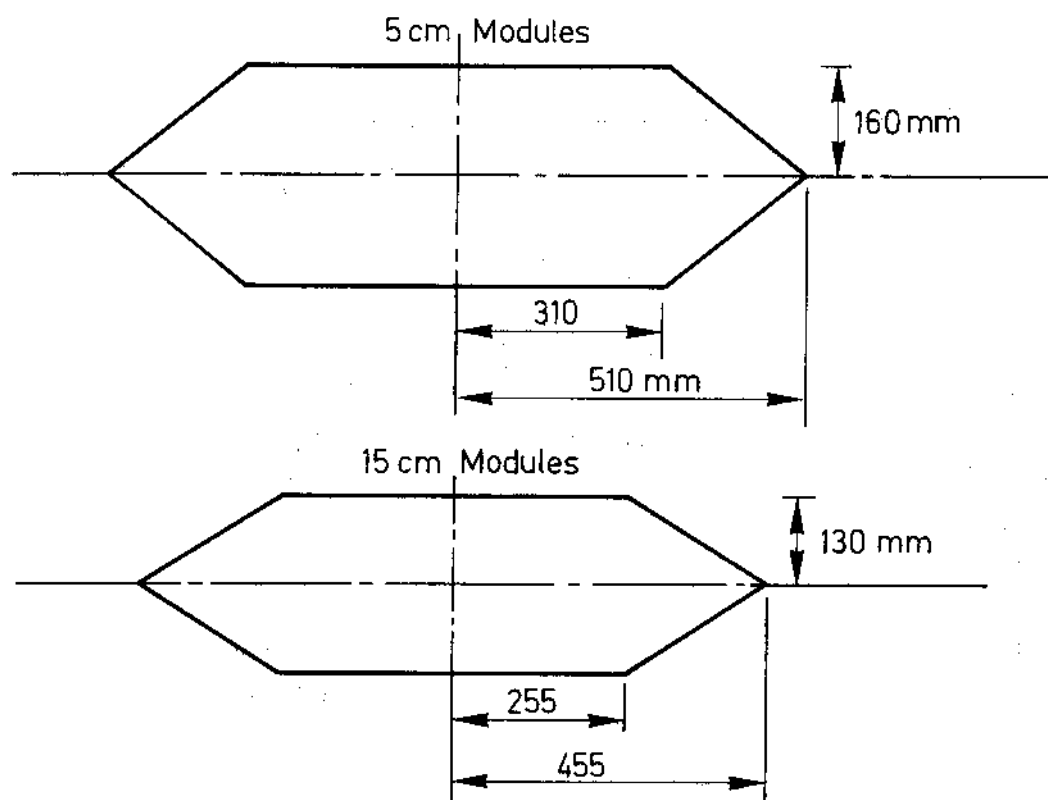


Fig. 5

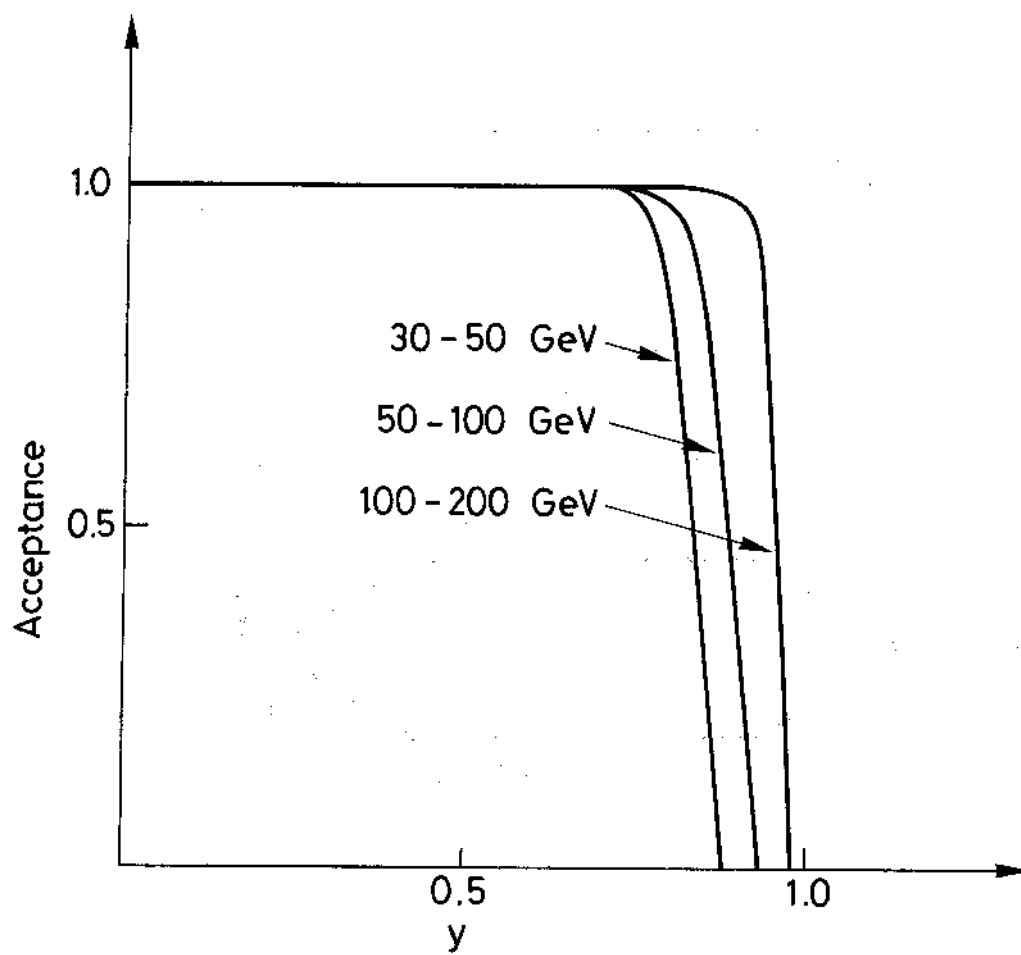


Fig. 6

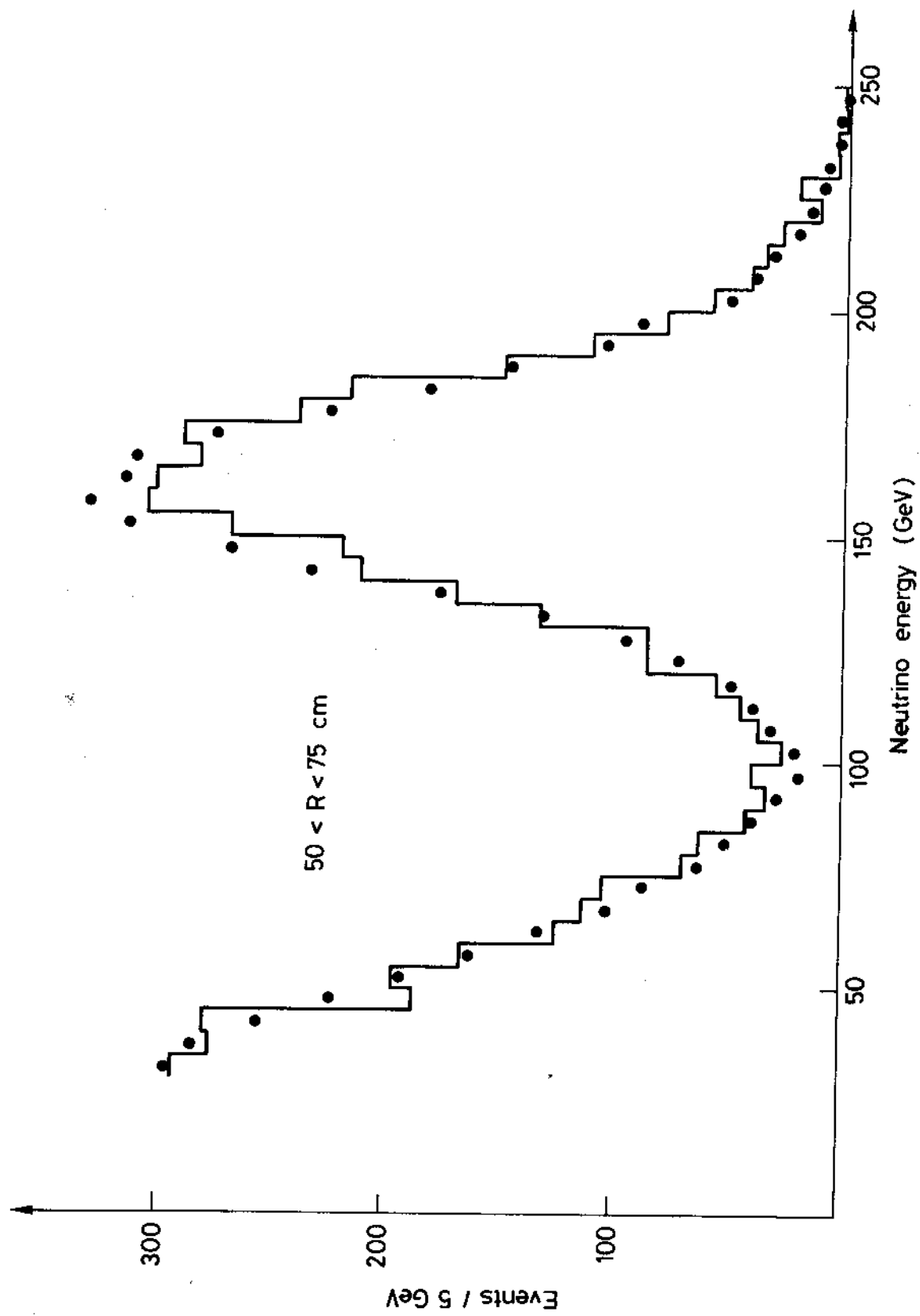


Fig. 7

Fig. 8

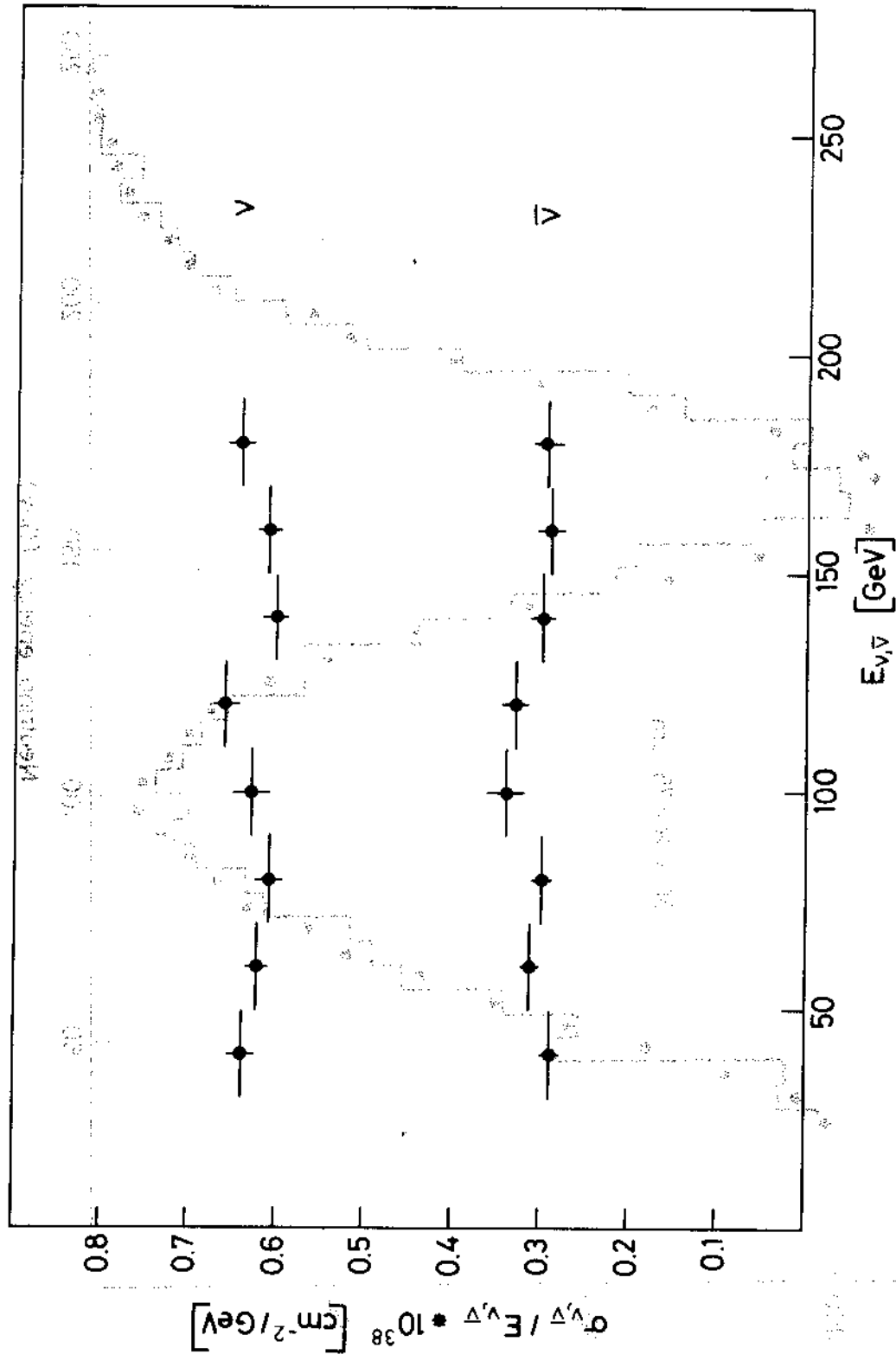


Fig. 8

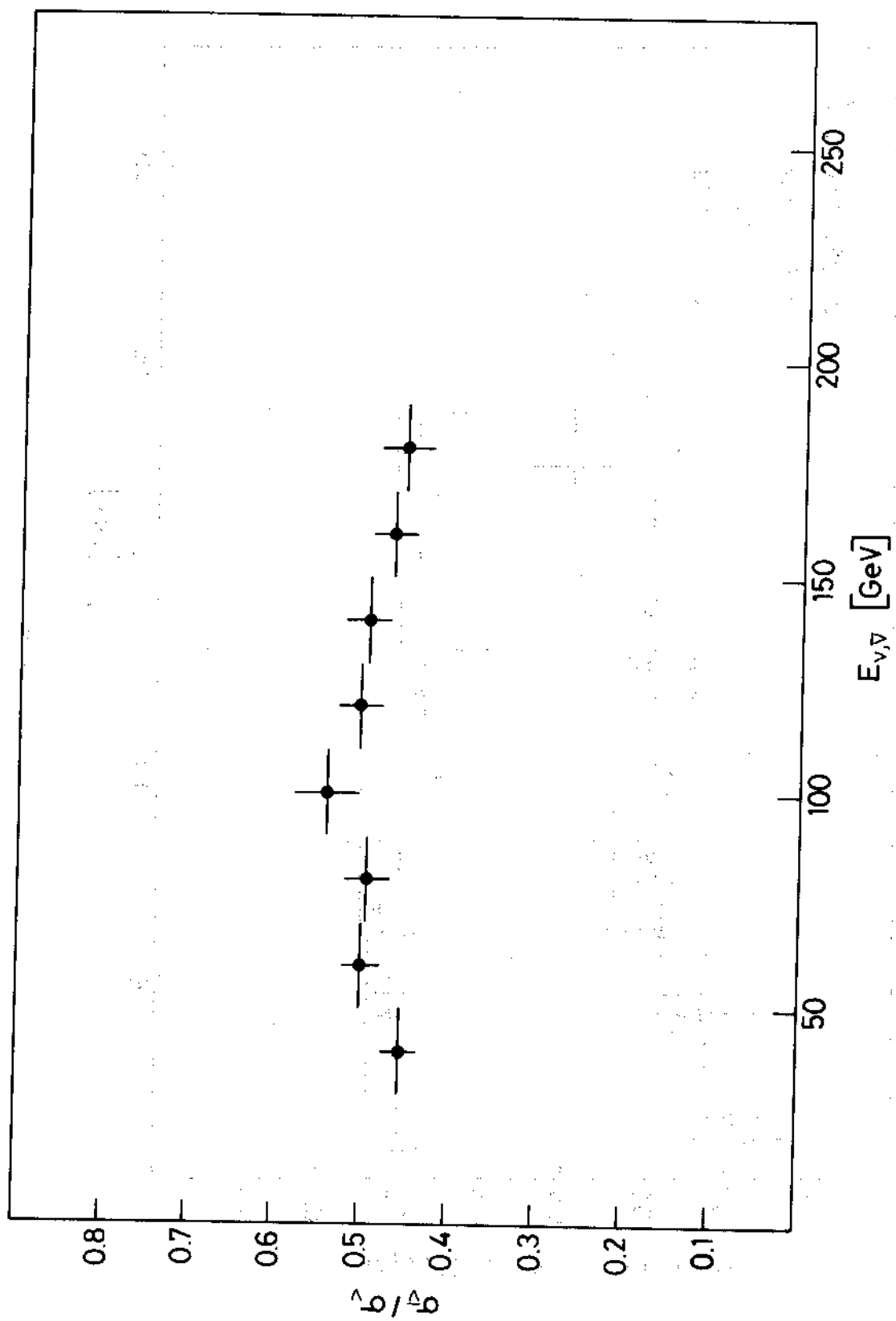


Fig. 9

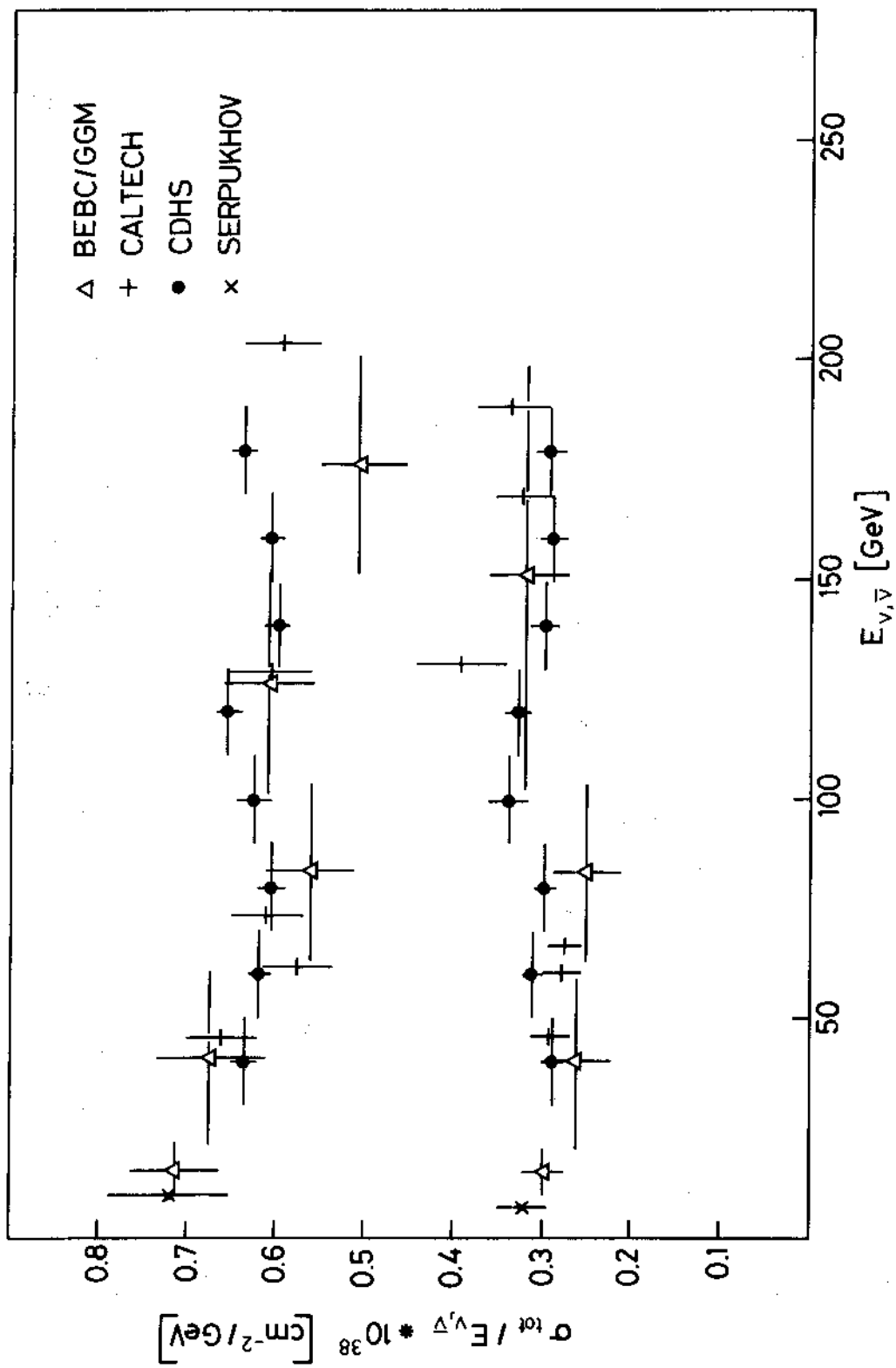


Fig. 10.

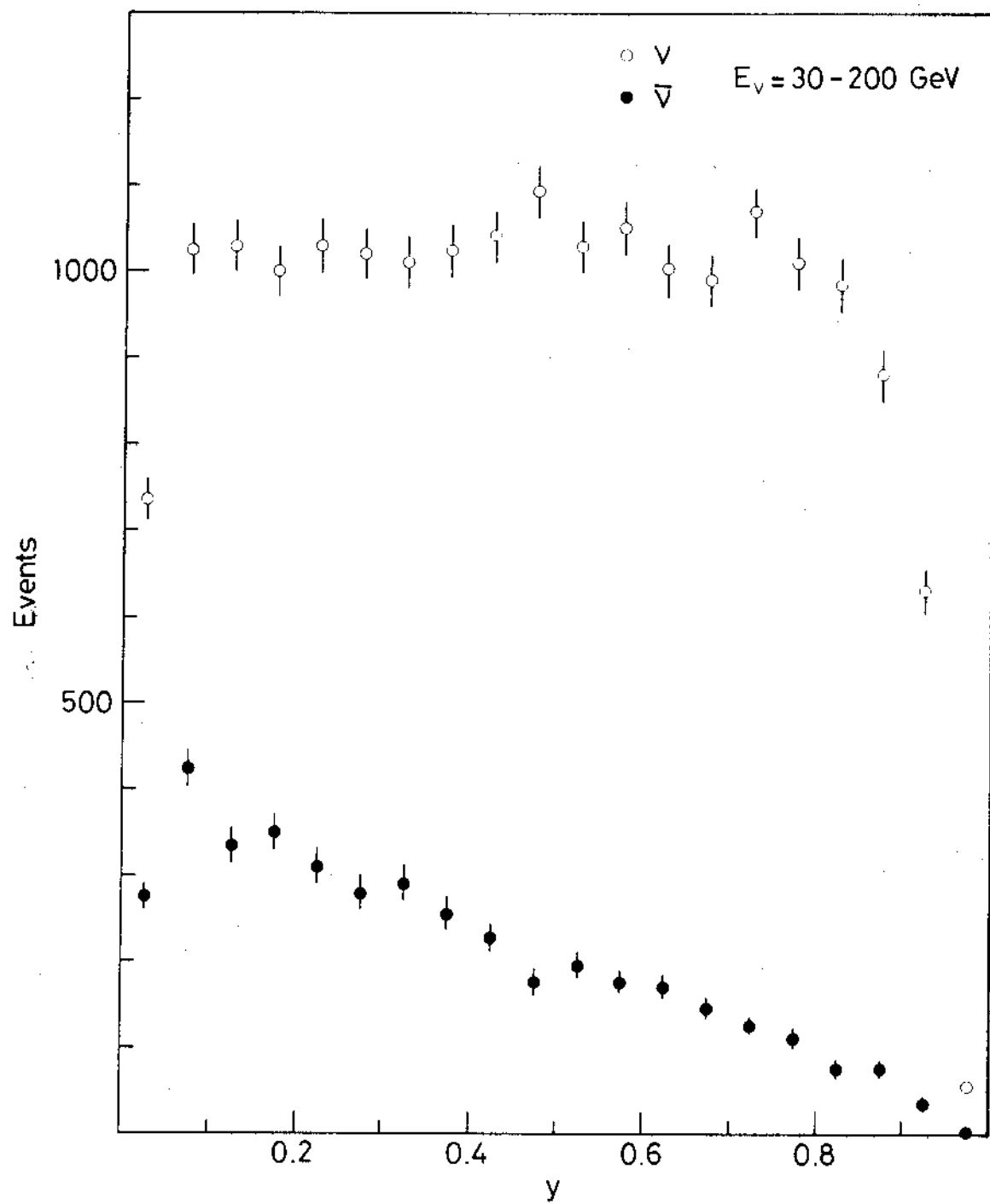


Fig. 11

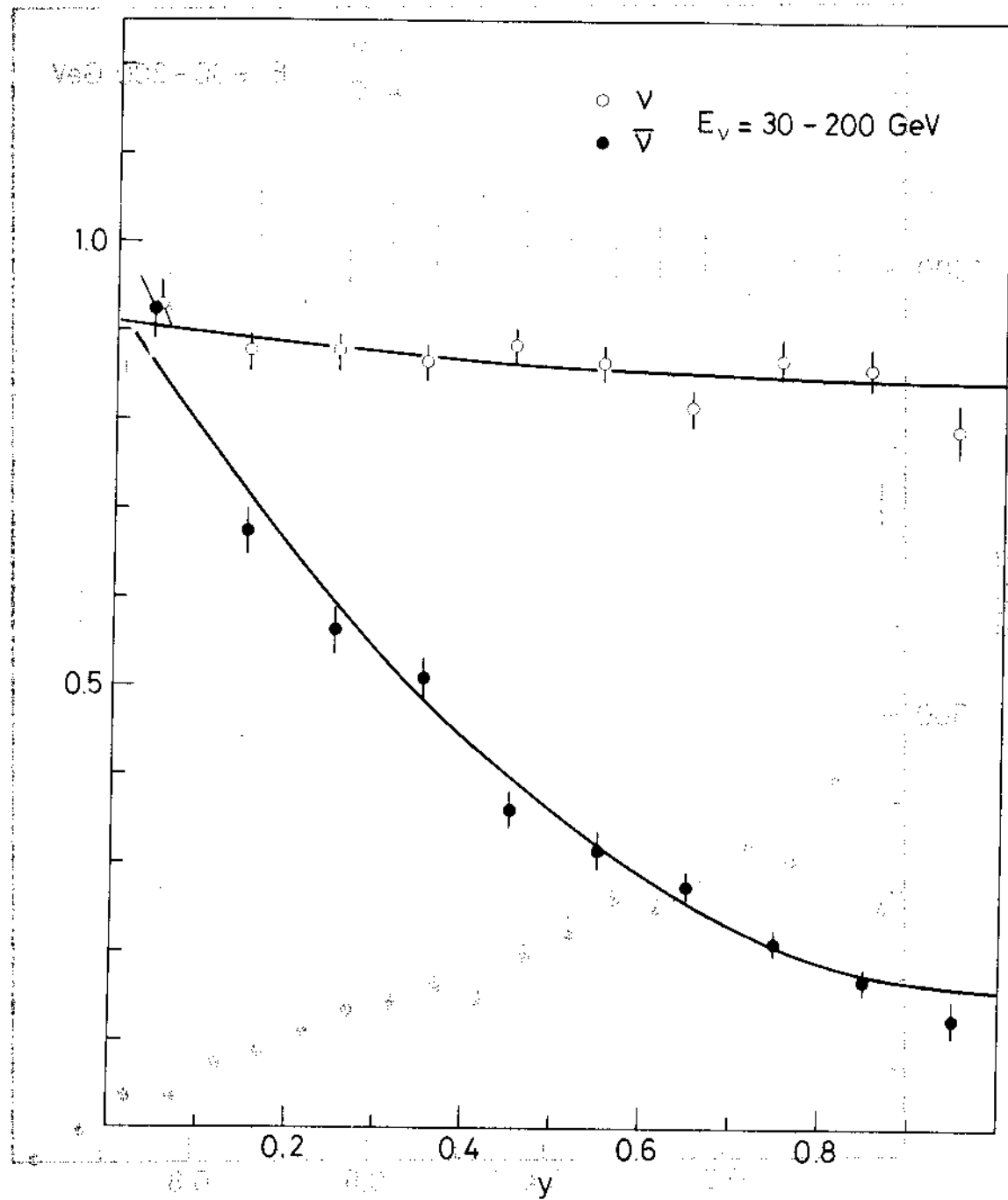


Fig. 12

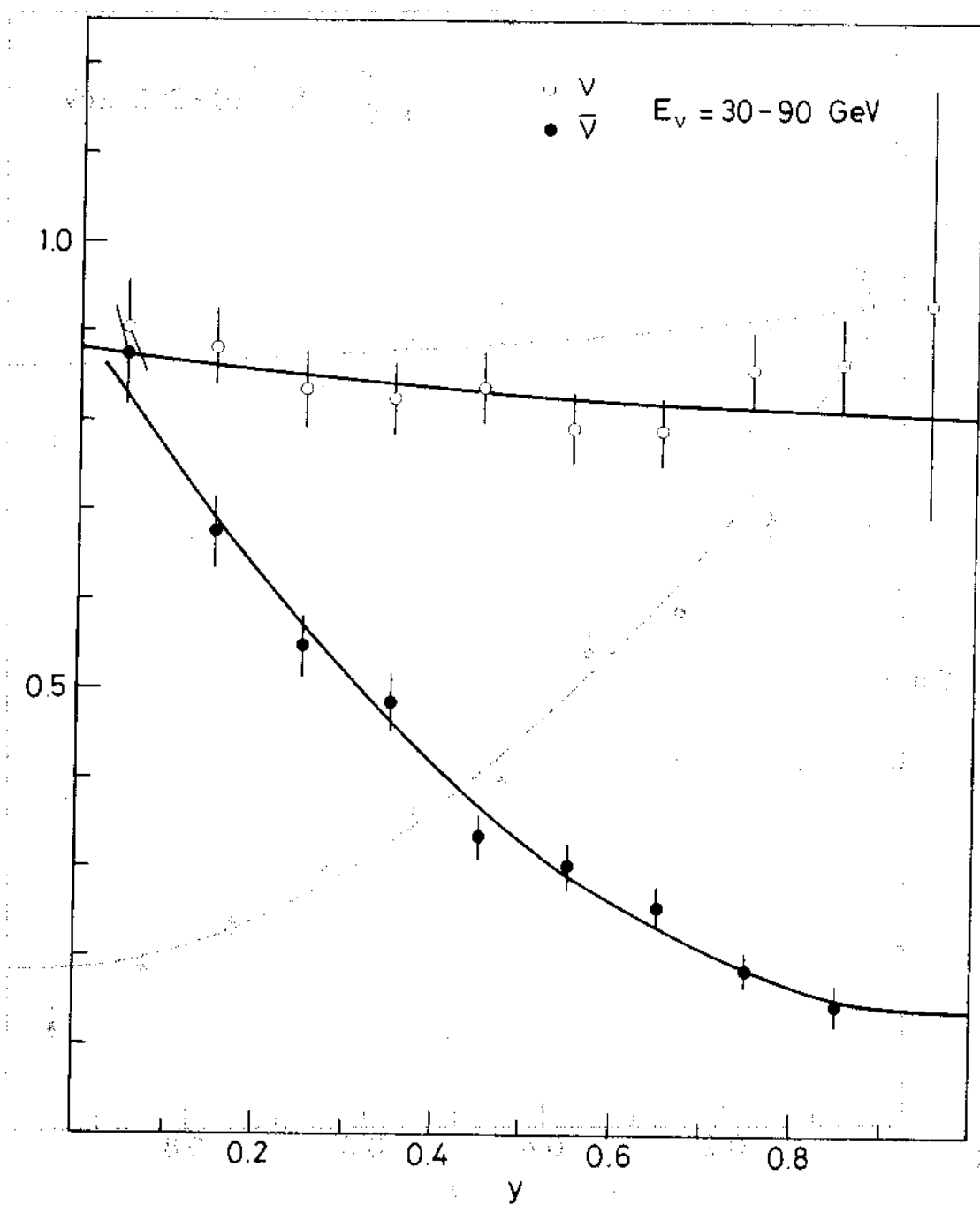


Fig. 13

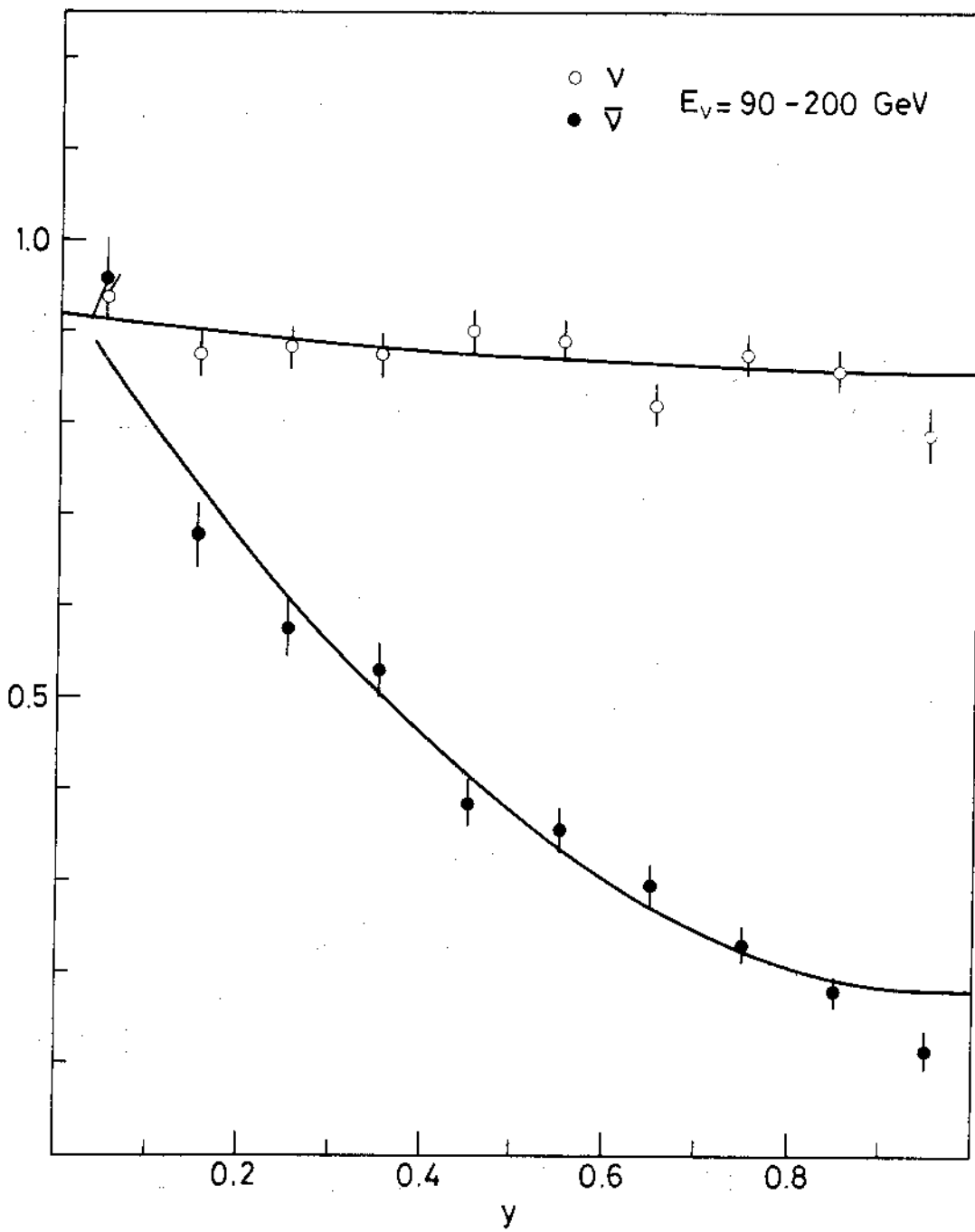


Fig. 14

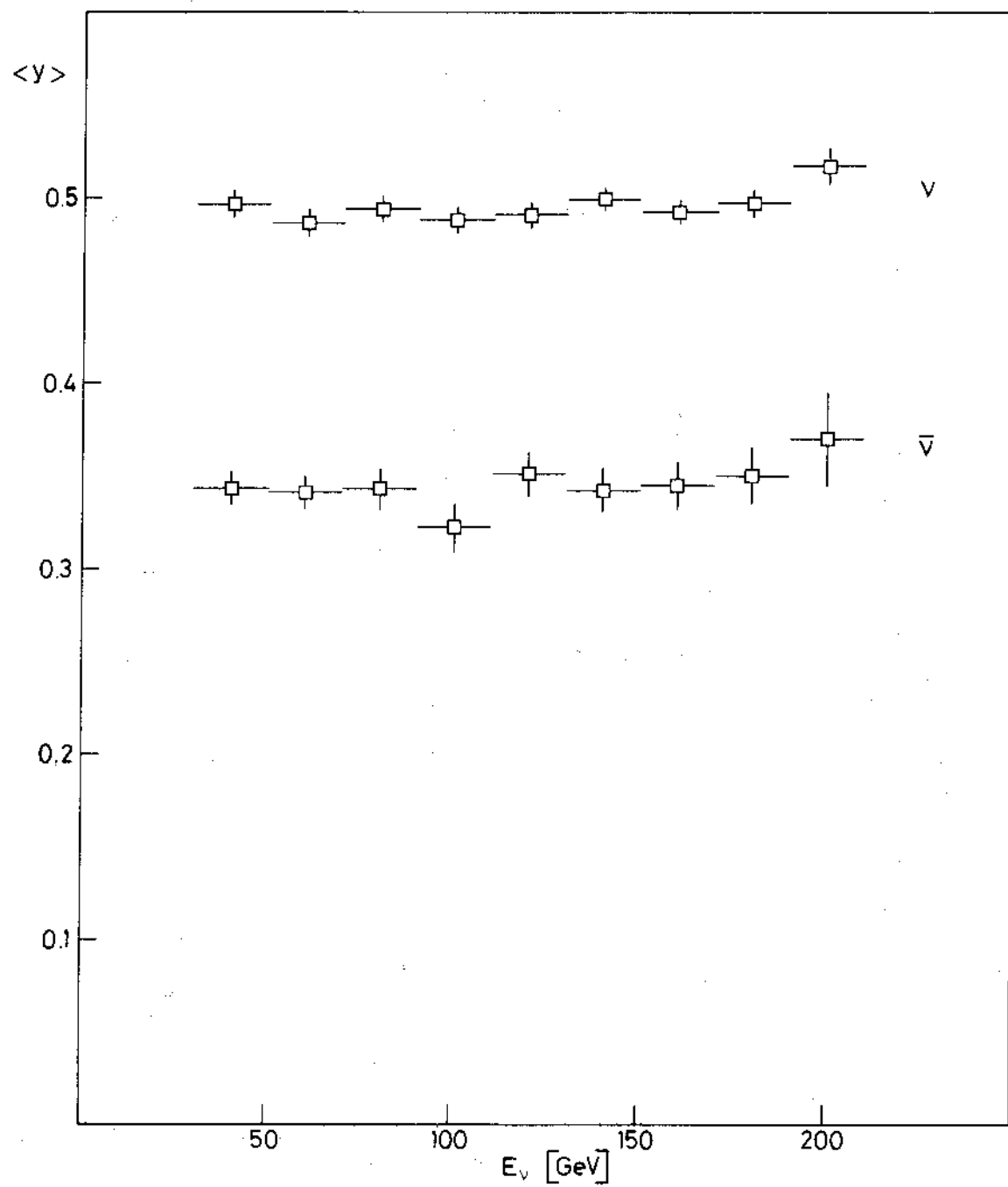


Fig. 15

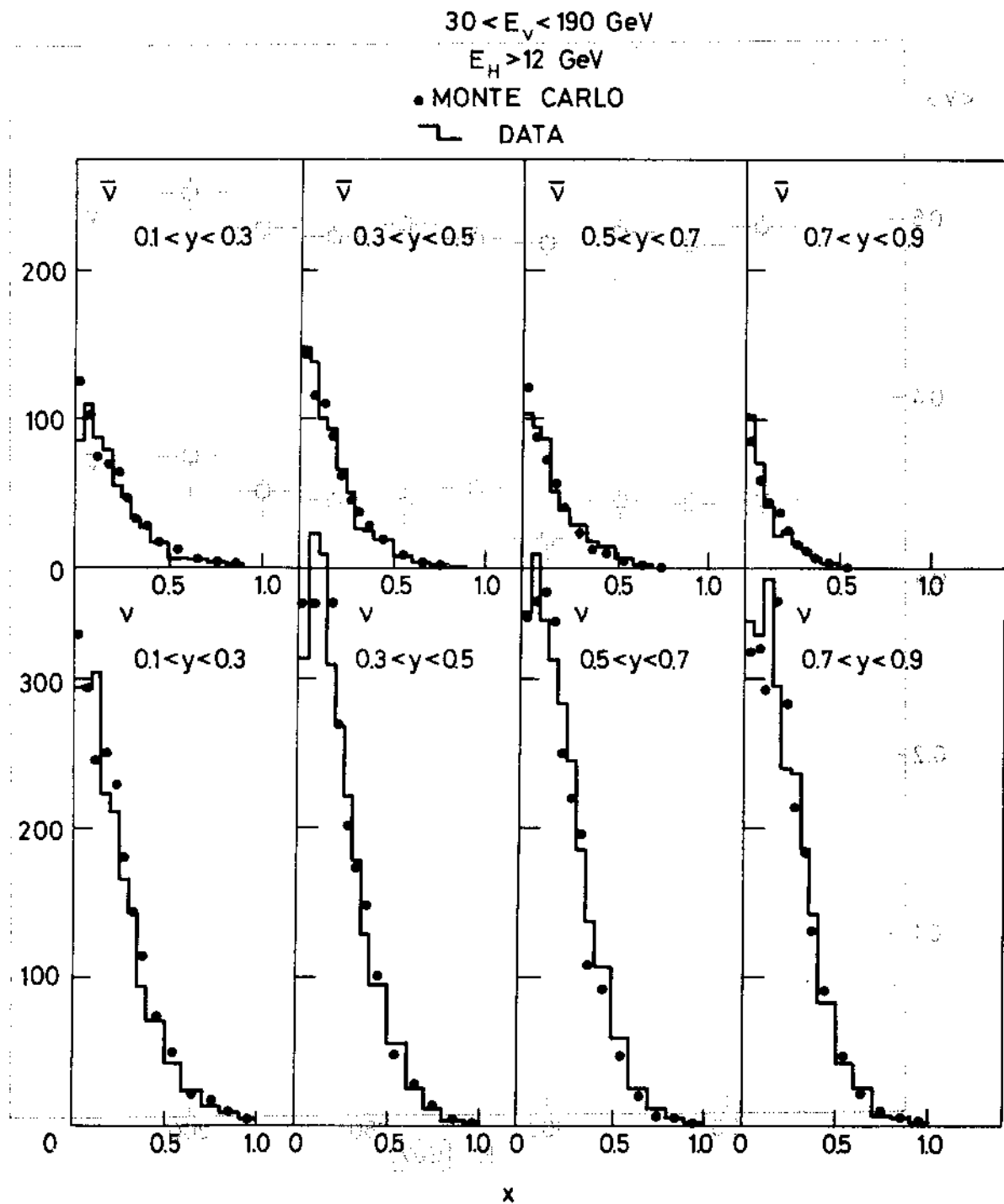


Fig. 16

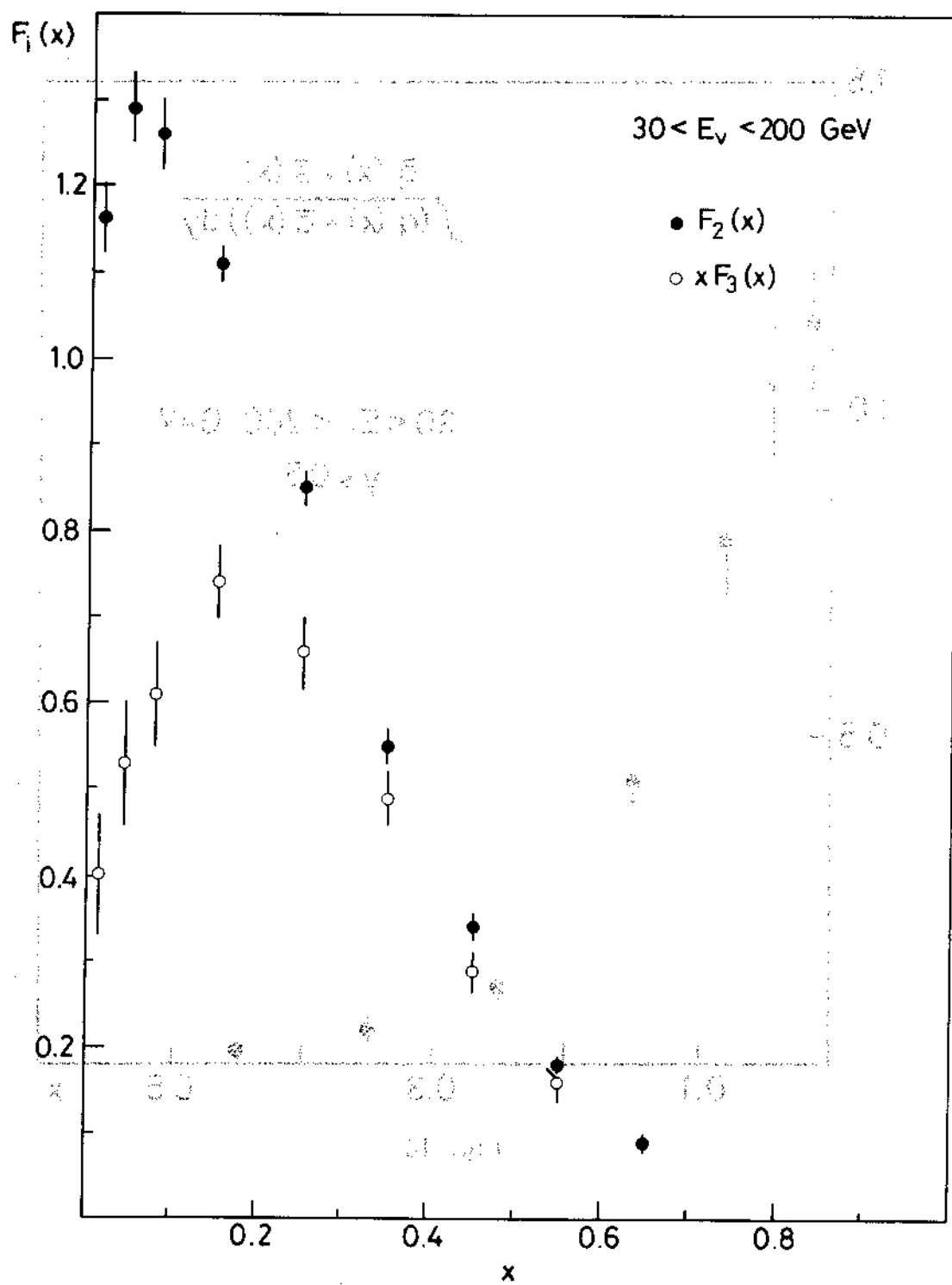


Fig. 17

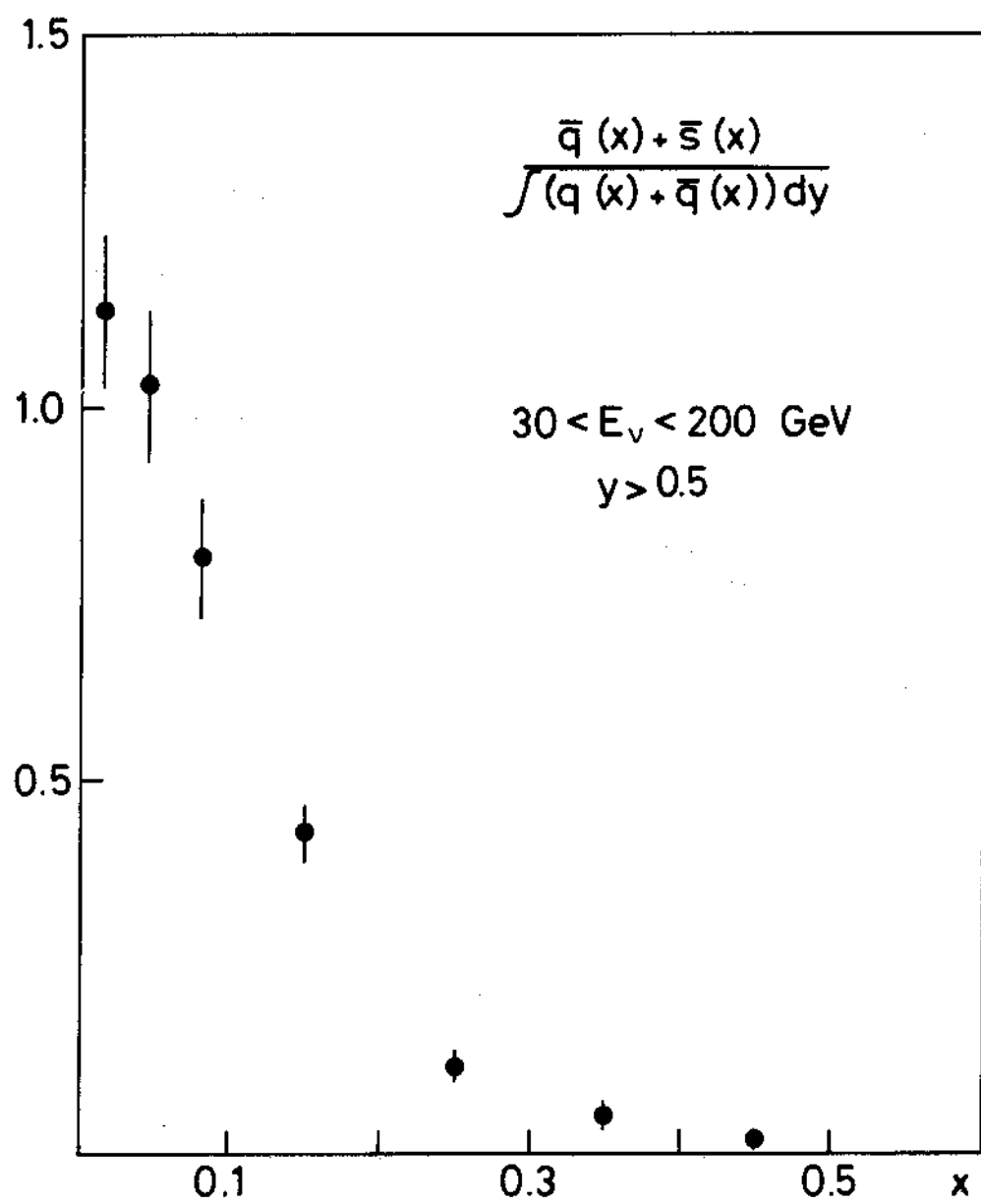


Fig. 18

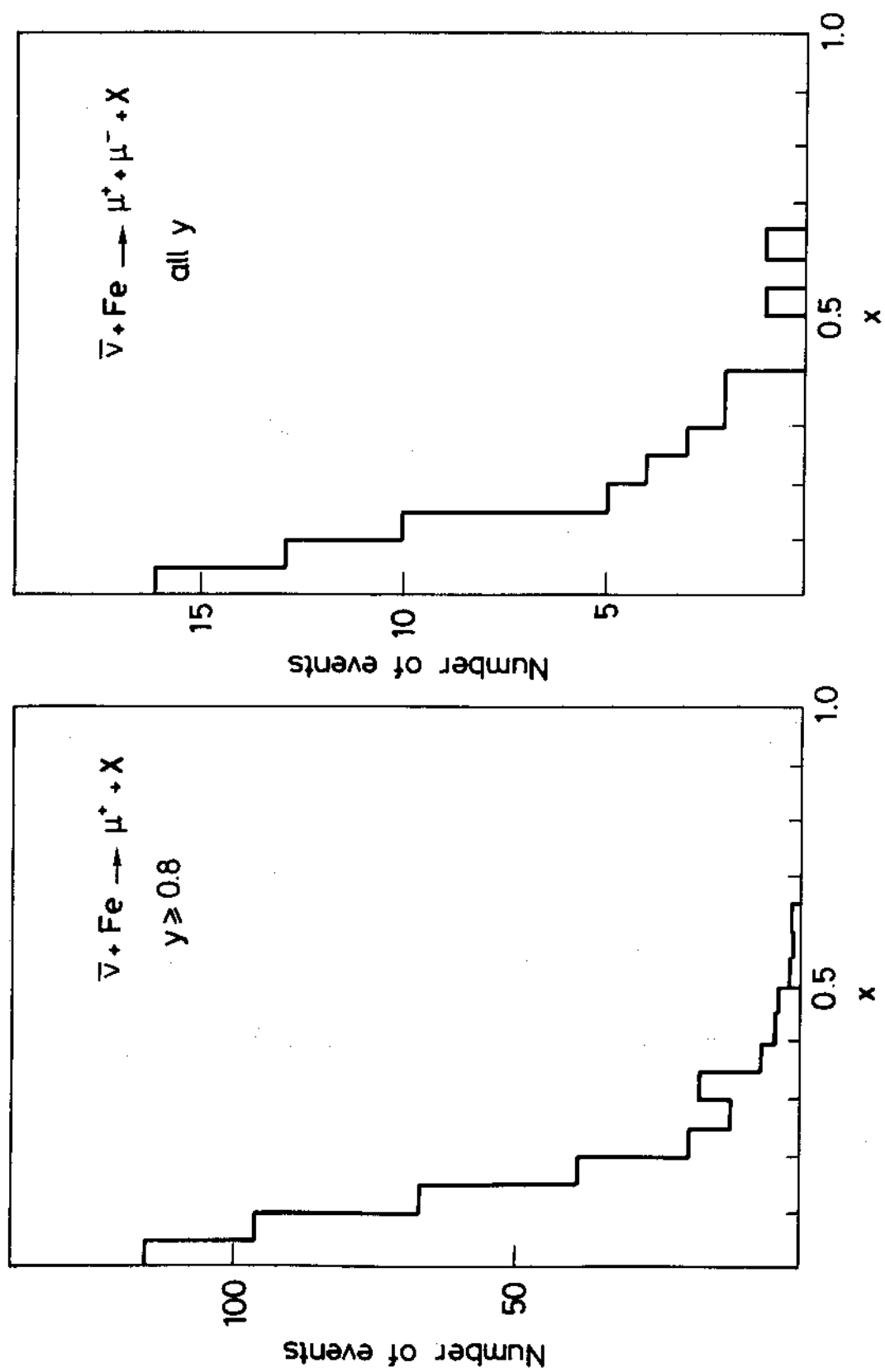
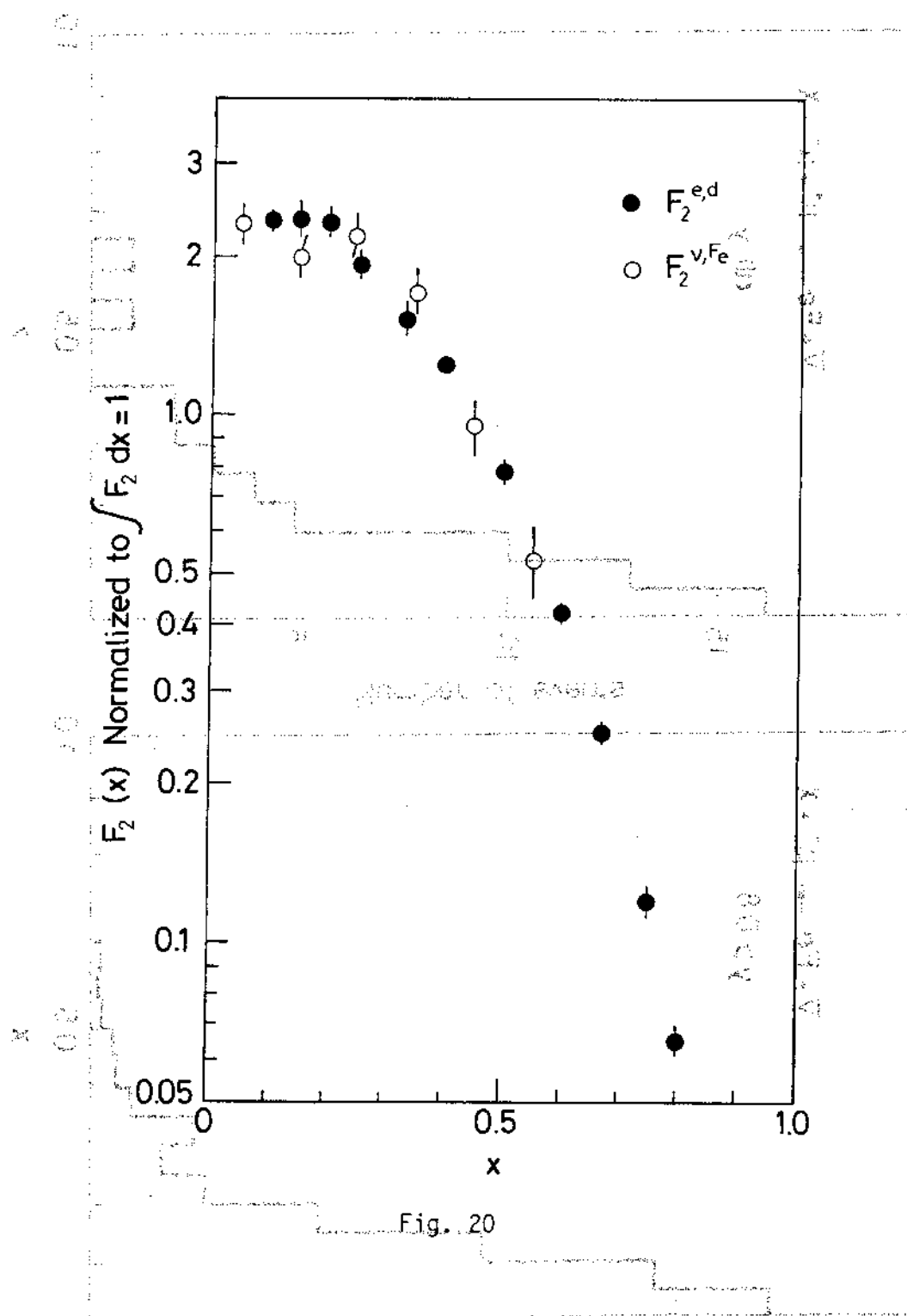


Fig. 19



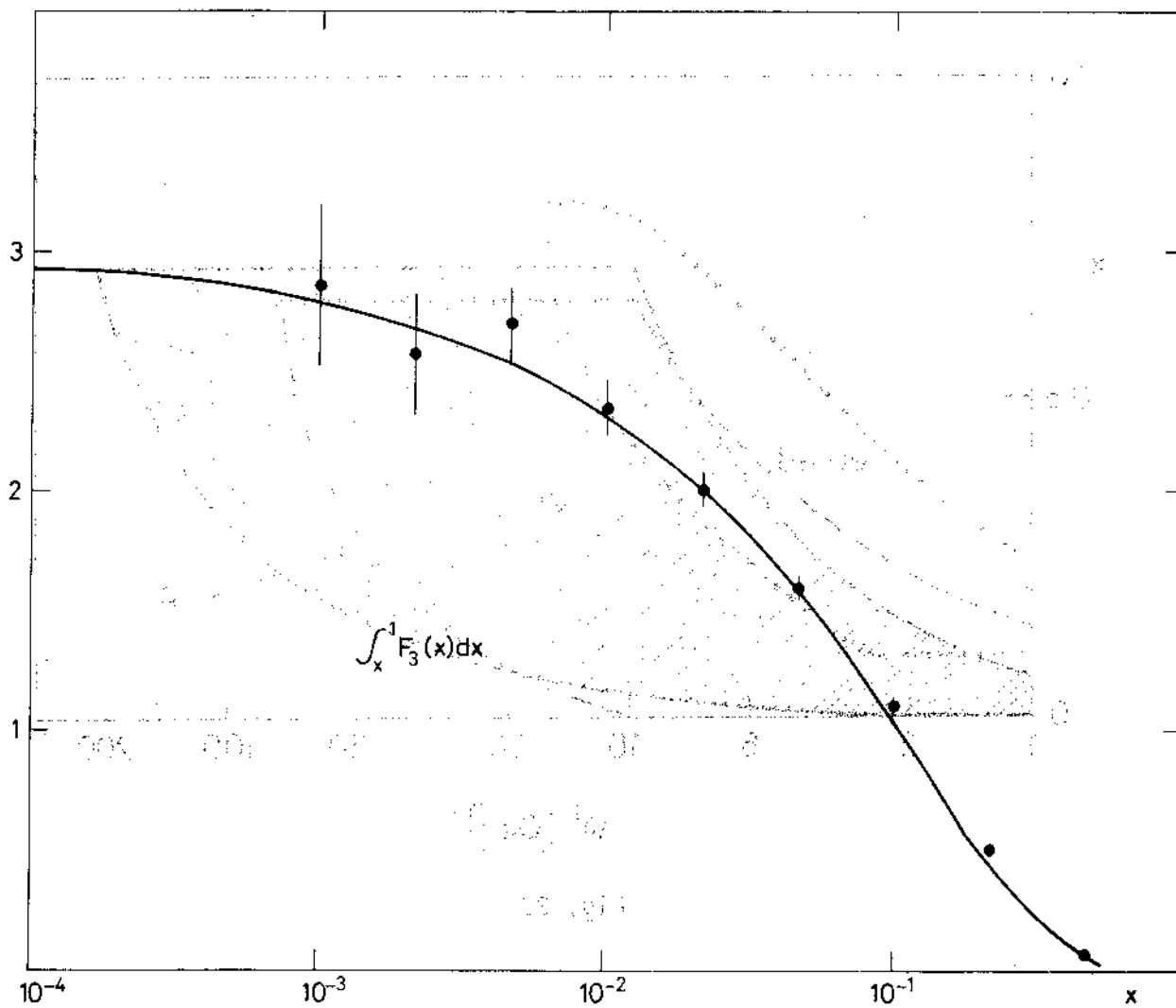


Fig. 21

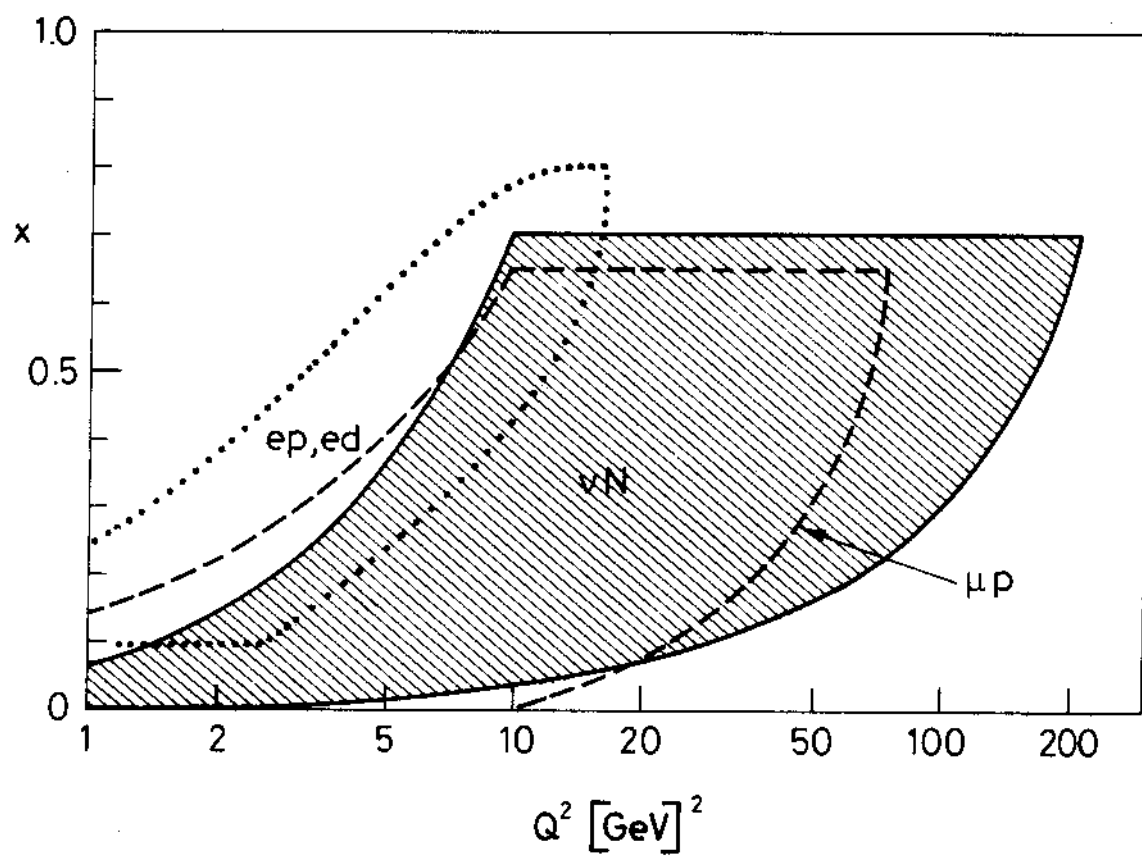


Fig. 22

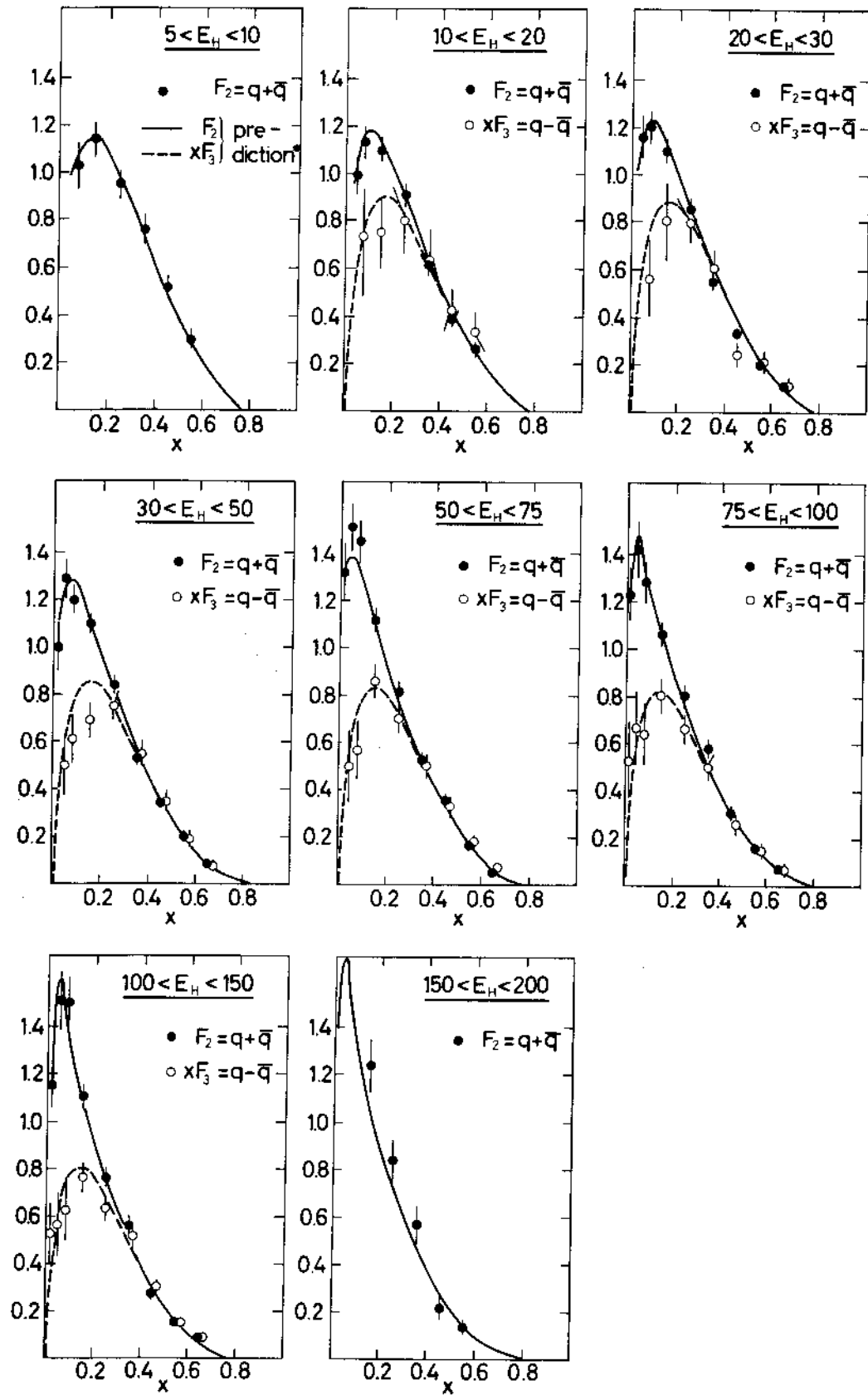


Fig. 23

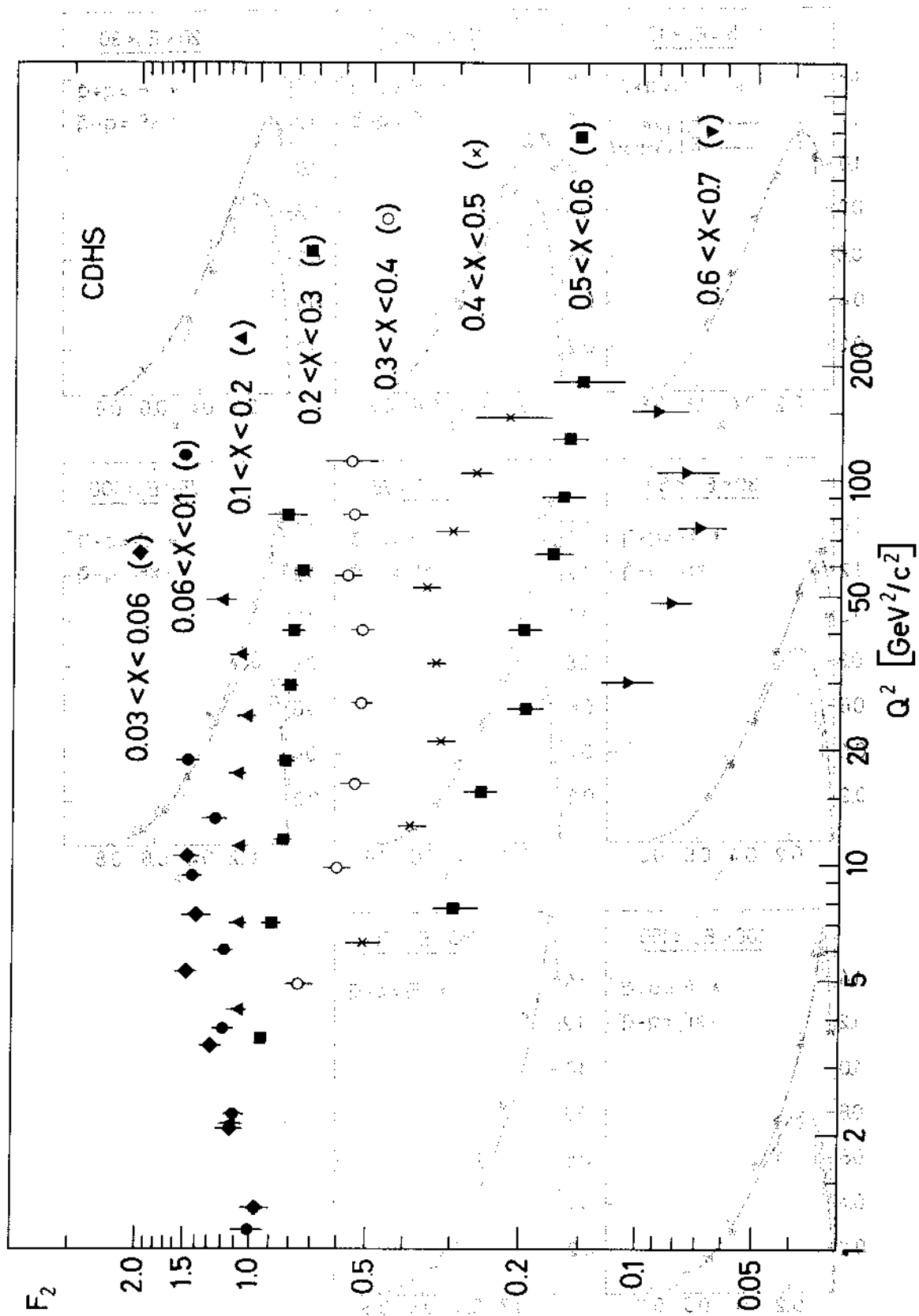


Fig. 24

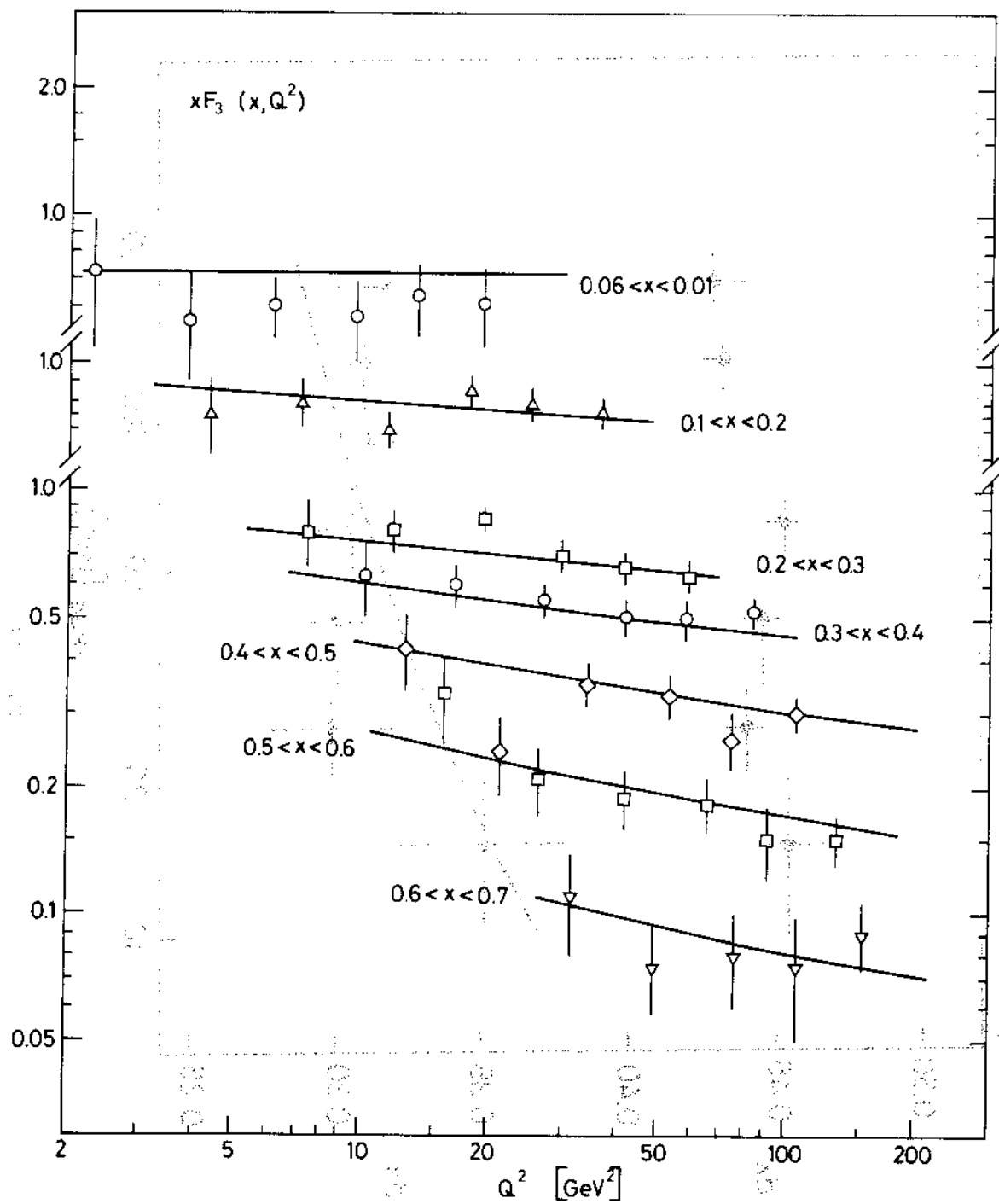


Fig. 25

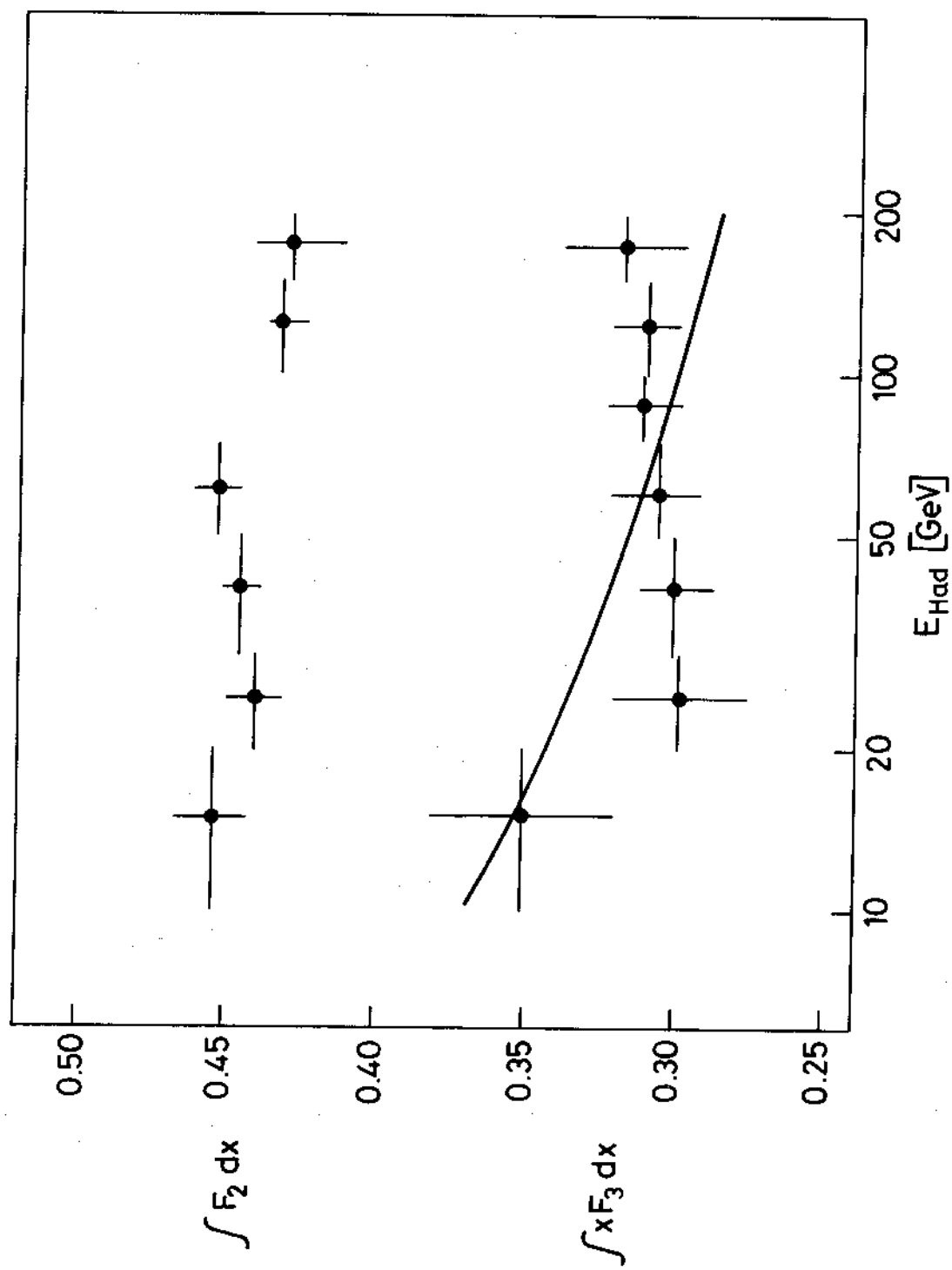


Fig. 26

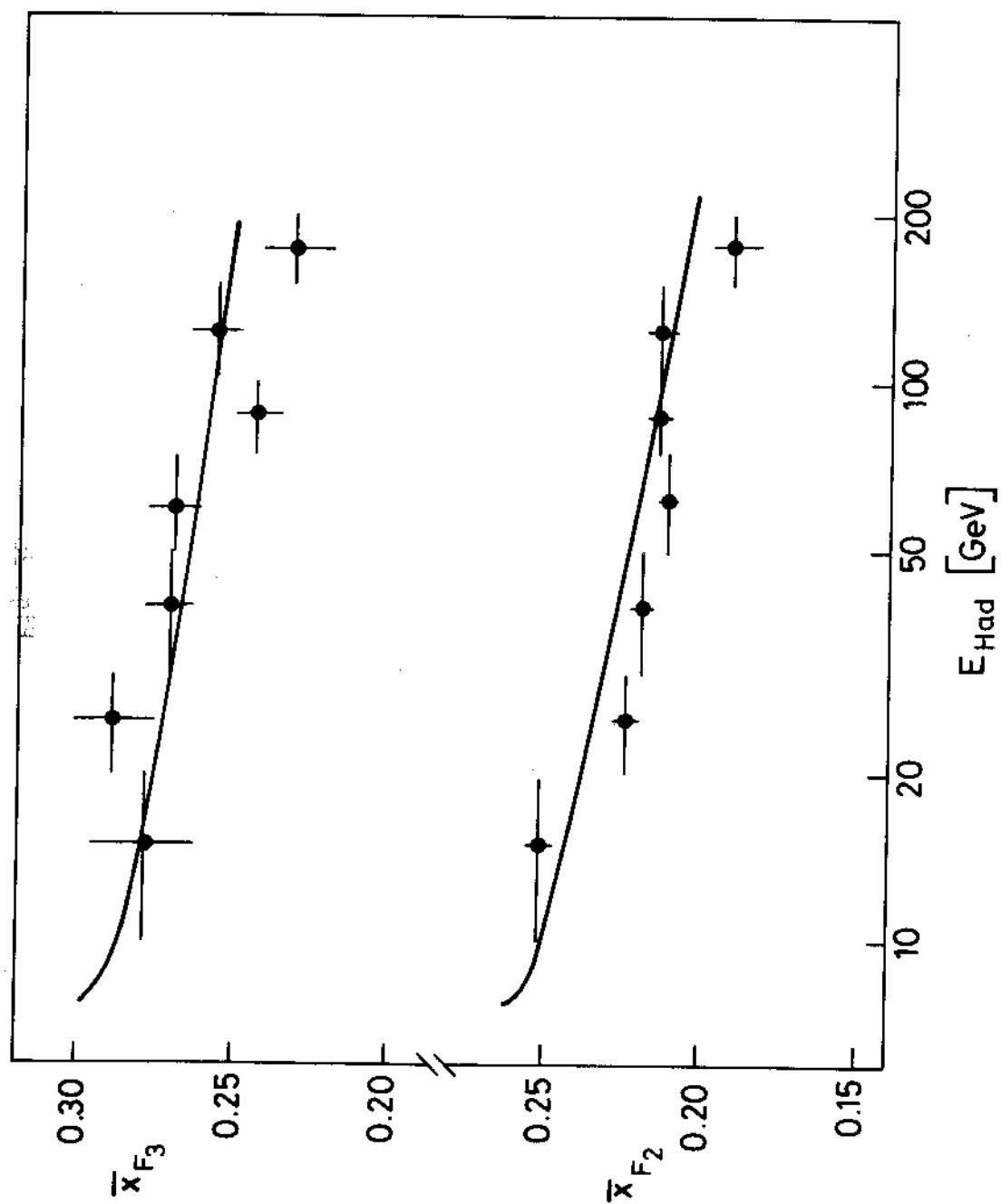


Fig. 27

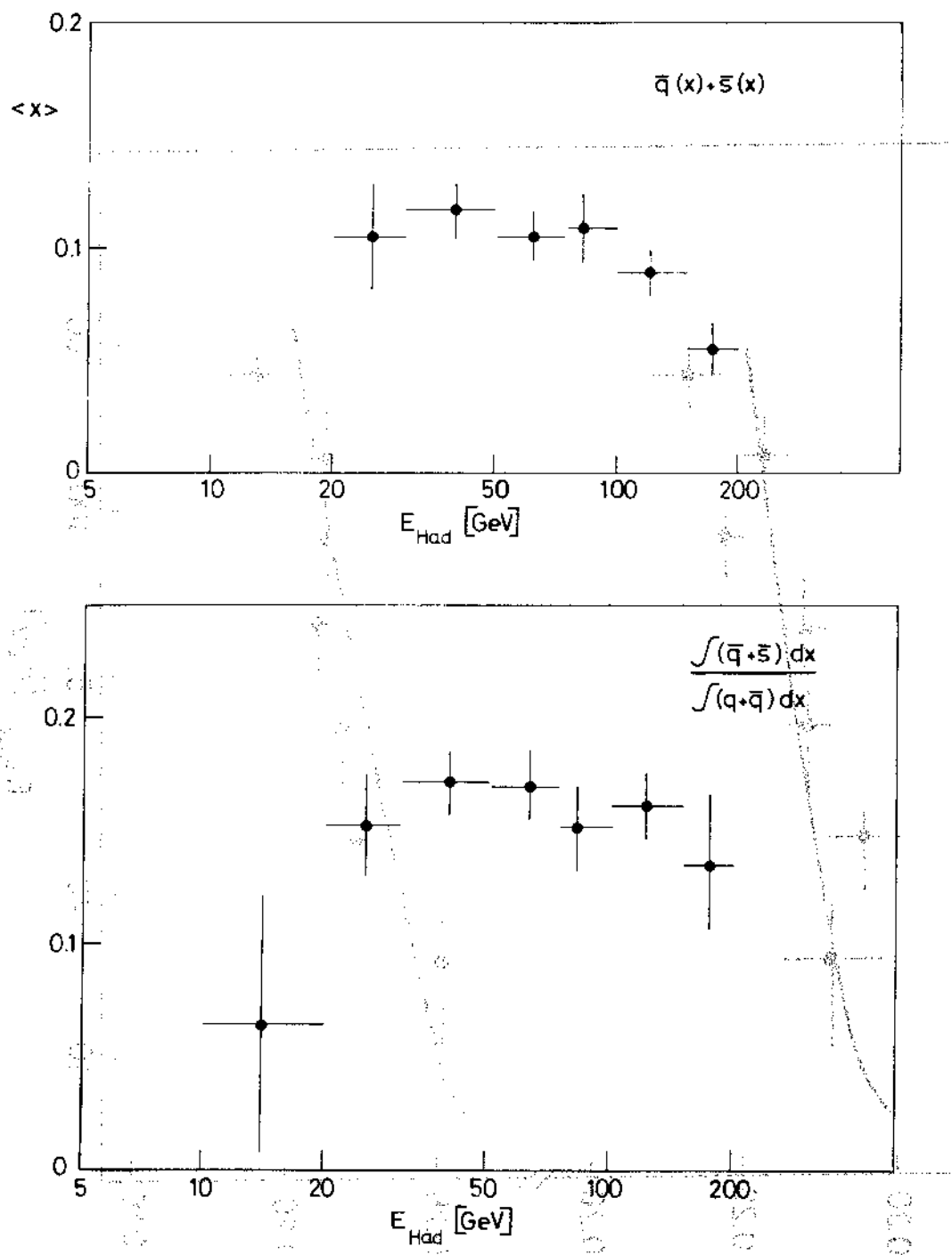


Fig. 28

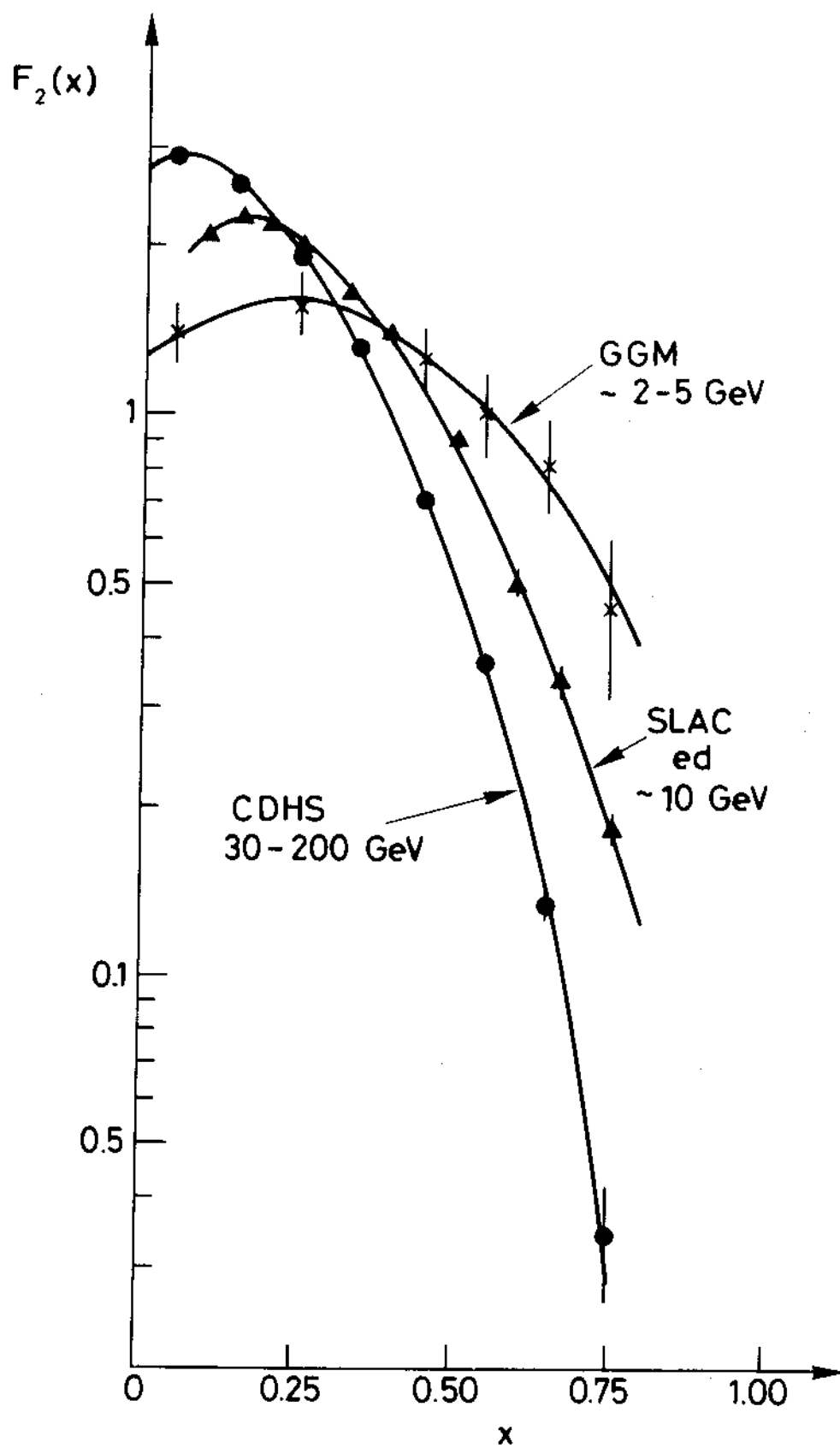


Fig. 29

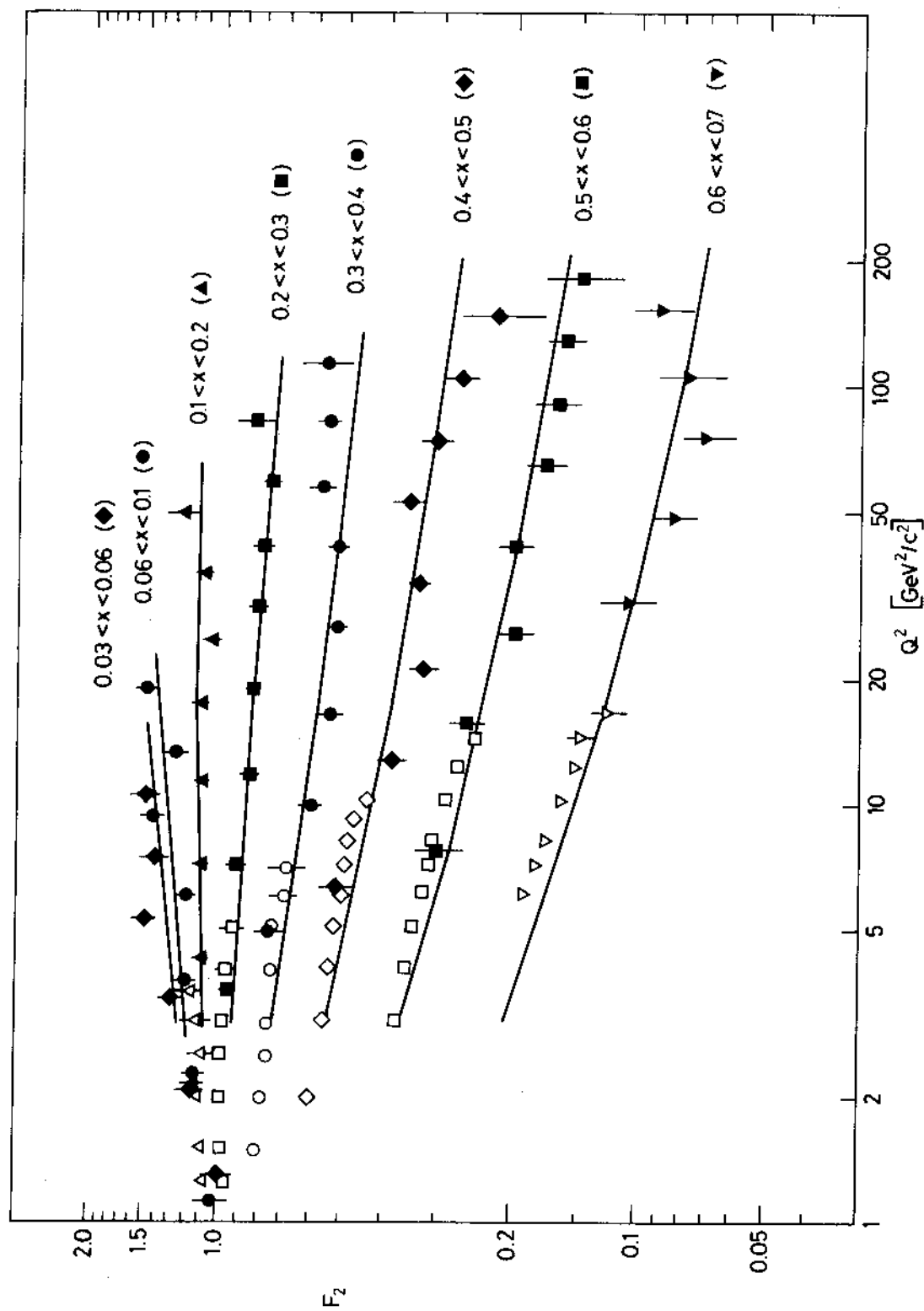


Fig. 30